博 士 論 文
（Doctoral Thesis）

(100) Oriented Poly-Si Thin Film Formation and Ultrahigh-Performance Poly-Si Thin Film Transistor Fabrication with Multi-Line Beam Continuous-Wave Laser Lateral Crystallization

（マルチライン連続発振レーザ・ラテラル結晶化による
(100)面方位制御多結晶シリコン薄膜形成と
高性能多結晶シリコン薄膜トランジスタの作製）

Nguyen Thi Thuy

広島大学大学院先端物質科学研究科
（Graduate School of Advanced Sciences of Matter
Hiroshima University）

2018 年 3 月
（March 2018）

目次

1. 主論文

(100) Oriented Poly-Si Thin Film Formation and Ultrahigh-Performance Poly-Si Thin Film Transistor Fabrication with Multi-Line Beam Continuous-Wave Laser Lateral Crystallization

（マルチライン連続発振レーザ・ラテラル結晶化による(100)面方位制御多結晶シリコン薄膜形成と高性能多結晶シリコン薄膜トランジスタの作製）

2. 公表論文

(1) Ultrahigh-performance (100)-oriented polycrystalline silicon thin-film transistors and their microscopic crystal structures
Thi Thuy Nguyen, Mitsuhisa Hiraiwa, and Shin-Ichiro Kuroki
Applied Physics Express, **10**(5), 056501-1 -056501-4 (2017).

(2) Characterization of (100)-Dominantly Oriented Poly-Si Thin Film Transistors using Multi-Line Beam Continuous-Wave Laser Lateral Crystallization
Thuy Thi Nguyen, Mitsuhisa Hiraiwa, Tatsuaki Hirata, and Shin-Ichiro Kuroki,
ECS Transactions, **75**(10), 49-54 (2016).

(3) Formation of (100) Oriented Large Poly-Si Thin Films with Multi-Line Beam Continuous-Wave Laser Lateral Crystallization
Thi Thuy Nguyen, Mitsuhisa Hiraiwa, Tomoyuki Koganezawa, Satoshi Yasuno, and Shin-Ichiro Kuroki,
Japanese Journal of Applied Physics, **57**(3), 031302-1-031302-6 (2018).

3. 参考論文

(1) Creating a Multiband Perfect Metamaterial Absorber at K Frequency Band Using Defects in the Structure
Manh Cuong Tran, Thi Thuy Nguyen, Tuan Hung Ho, and Hoang Tung Do
Journal of Electronic Materials, **46**(1), 413-417 (2016).

(2) Influence of Structural Parameters on a Novel Metamaterial Absorber Structure at K-band Frequency
Tran Manh Cuong, Nguyen Thi Thuy, and Le Anh Tuan
Journal of Electronic Materials, **45**(5), 2591-2596 (2016).

主 論 文

Contents

Chapter 1: Introduction

1.1 Background

1.1.1 Low temperature poly-Si thin film transistors

Thin film transistors (TFTs) have been a key technology for developing active matrix flat panel displays (AM-FPDs) for over 30 years. Since 1980s, a-Si:H TFTs have been applied in manufacturing large area mass displays. They however have a low electron field effect mobility (μ_{eff}) of < 1 $cm^2V^{-1}s^{-1}$[1]. Since 1990s, the TFTs for mobile displays have been highly demanded to have a high μ_{eff}, and research and development on poly-Si TFTs and oxide TFTs have been progressed. A-IGZO TFTs have more advantages due to simple process and can be fabricated at room-temperature. Their μ_{eff} of ~ 10 $cm^2V^{-1}s^{-1}$ is high enough for LCDs and OLEDs of desk top displays and TVs [2,3]. For high resolution mobile displays and digital processing applications such as system on panel (SOP), three-dimensional (3D) electronics, and integrated circuits (ICs), high performance low temperature poly-Si (LTPS) TFTs with high μ_{eff} of more than 100 $cm^2V^{-1}s^{-1}$ have greater advantages. The poly-Si TFTs' performance has been continuously enhanced by the progress of many crystallization methods such as excimer laser annealing (ELA), sequential lateral solidification (SLS), solid-phase crystallization (SPC), plasma jets, and continuous-wave laser lateral crystallization (CLC) [4-10]. Among these technologies, the CLC is a promising technology because it is a simple method to form large crystal grains growing along laser scanning direction. These grains are larger than feature size of devices and their boundaries are parallel to current flow. Hence, the effect of grain boundaries on device performance becomes insignificant. Utilizing the CLC, high-performance TFTs with μ_{eff} of 566 $cm^2V^{-1}s^{-1}$ have been achieved [11]. On the other hand, nanowire TFTs fabricated on the CLC poly-Si films had excellent field effect mobility of up to 900 $cm^2V^{-1}s^{-1}$ because these TFTs were patterned in single crystal grains and were considered as single-crystal TFTs [12]. However, the CLC poly-Si thin films have random orientation resulting from the Gaussian distribution of laser beam. The performance of the TFTs fabricated on these films is remarkably different. For dealing with this disadvantage, controlling the preferential orientation of the poly-Si thin films plays a very important role. Among mobility anisotropy of carriers, (100) crystals provide the highest electron mobility and lowest hole mobility. In addition, the poly-Si TFTs have

advantages comparing to bulk silicon devices due to high tensile strain induced in the poly-Si thin films. Therefore, (100) preferentially oriented poly-Si thin films would provide excellent TFTs.

1.1.2 Electron and hole mobility dependence on crystal orientation

It is widely known that the mobility of carriers is anisotropic in semiconductor devices because of the anisotropy of electron and hole effective mass and the difference of density of states at the Si/SiO_2 interface between crystal orientation. The most important factor is the effective mass of the carriers.

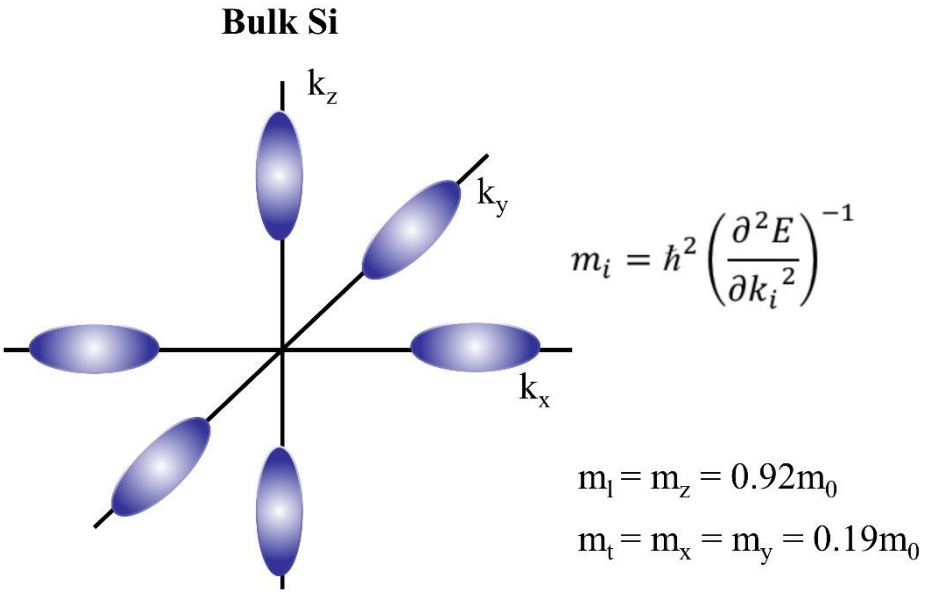

Fig. 1.1 Shape of conduction band valleys of silicon as constant energy surfaces in k-space.

Unconfined bulk silicon conduction band consists of sixfold degenerate valleys as shown in Fig. 1.1. Each isoenergy ellipsoid has longitudinal effective mass $m_l = 0.92m_0$ and transverse effective mass $m_t = 0.19m_0$. Therefore, the effective mass is anisotropic among crystal orientations and predominately controls the mobility. The minimal average effective mass is along principle axes.

Table 1 Characteristics of Si crystal planes

Orientation	Plane area of unit cell (cm^2)	Atoms in area	Available bonds in area	Atoms/cm^2	Available bonds/cm^2
<100>	a^2	2	2	6.8×10^{14}	6.8×10^{14}
<110>	$\sqrt{2}a^2$	4	4	9.6×10^{14}	9.6×10^{14}
<111>	$\sqrt{3}a^2$	2	3	7.85×10^{14}	11.8×10^{14}

The second important factor is the density of states at the interface (D_{it}) related to available bonds per unit area on the silicon surface. The characteristics of (100), (110), and (111) oriented Si crystal planes are listed in Tab. 1. It appears that the (100) surface has the smallest number of available bonds [19-20].

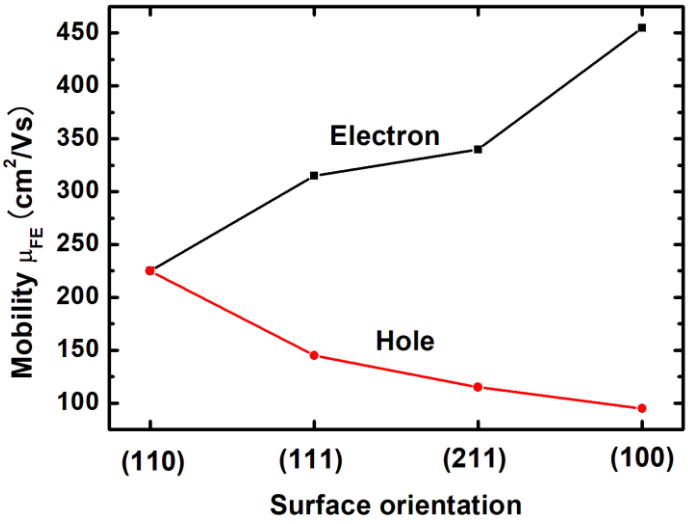

Fig. 1.2 Field effect mobility of electron and hole as functions of surface orientation in MOSFETs [14].

In silicon MOSFETs, the carrier mobility is dependent on the surface orientations of the substrate. It has been reported that μ(100) is higher than μ(111) and μ(011) for electron mobility and the ratio of μ(100)/ μ(110) is appropriately 2 for electron mobility shown in Fig. 1.1 [14]. Contrastingly the highest hole mobility appears on the (110) plane. It

decreases in the order of μ(110) > μ(111) > μ(011) for hole mobility. These orders of the mobility is in accordance with the order of calculated effective mass of carriers [13-18].

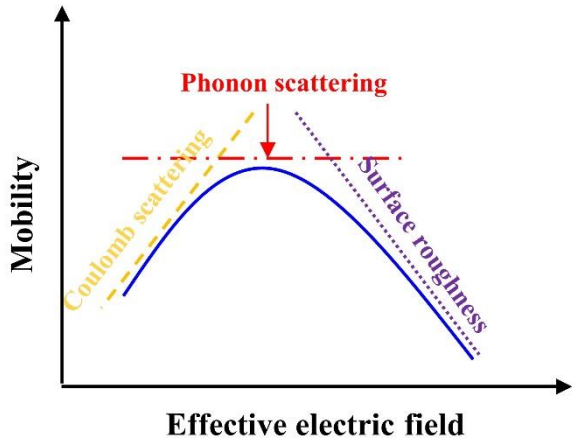

Fig. 1.3 Universal mobility curve of silicon MOSFETs

In addition, other parameters such as impurity concentration, temperature, and grain boundaries in polycrystalline semiconductors are remarkable factors that impact on the mobility [21-22]. Figure 1.3 shows the universal mobility curve of silicon MOSFETs. It can be divided into Coulomb scattering, phonon scattering, and surface roughness scattering. The mobility is limited by these scattering. Phonon scattering is dominant at high temperature. Surface roughness scattering becomes more dominant as the high effective field is applied. On the other hand, Coulomb scattering has a higher effect with higher impurity concentration.

1.1.3 Strain-induced energy band splitting and device performance enhancement

Strained-Si technology has been applied to improve the carrier mobility of MOSFETs. Strained-Si/Relaxed-SiGe has been a typical technology that has been developed for a previous decade. The band structure will be modified with band splitting and band warping. Tensile strain makes the conduction band energy splitting into two energy states of Δ_2 and Δ_4. It deduces the average electron effective mass via repopulation of Δ_2 shown in Fig. 1.4. In addition, if the energy splitting between Δ_2 and Δ_4 valleys becomes larger

than optical phonon energy (~60 meV for Si), intervalley phonon scattering is effectually repressed. Therefore, the mobility is significantly enhanced due to a decrease in average conductivity mass and a suppression in intervalley scattering [23-26].

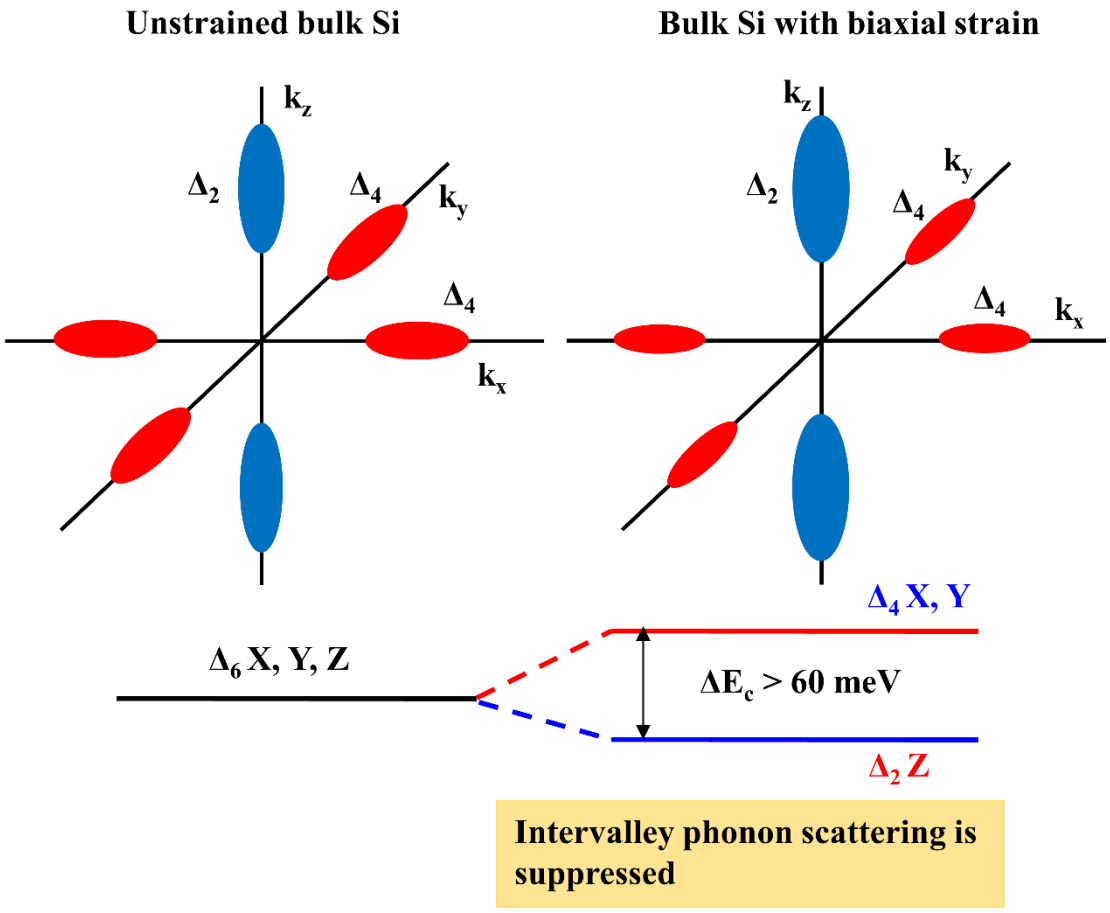

Fig. 1.4 Schematic of conduction band splitting in strained-Si.

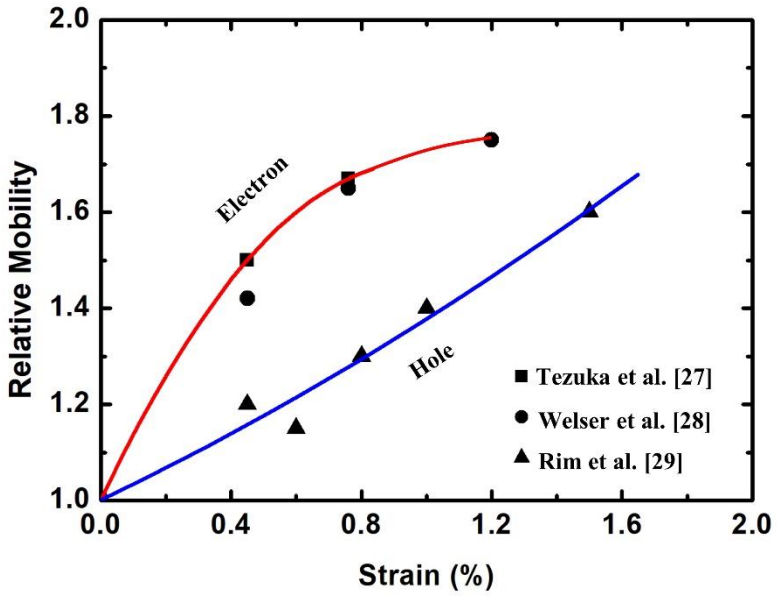

Fig. 1.5 Experimental electron and hole mobility enhancement in bulk Si devices [27-29].

It has been reported that the biaxial tensile strain significantly enhanced electron mobility and compressive strain enhanced hold mobility. With a biaxial tensile strain of 0.45%, the enhancement of electron mobility was up to 50% shown in Fig. 2(b). The electron mobility enhancement of uniaxial tensile strain is better than that of biaxial tensile strain .

1.2 Motivation and purpose

High-performance LTPS-TFTs have been a key goal for the continuous progress of the FPD technology and digital processing applications. With the advantage of high biaxial tensile strain poly-Si thin films, the electron mobility of the poly-Si TFTs has been expected to be higher than that of bulk Si devices. With high mobility TFTs, that are comparable to c-Si devices, their applications such as the SOP, 3D-electronics, and ICs glass sheet computers can be developed in the future. However, the TFTs' mobility has been limited due to the effects of grain boundaries of small crystal grains and uncontrollable crystal orientation. For high-performance poly-Si TFTs, grain size needs to be larger than the feature size of device's channels, and the surface crystal orientation of poly-Si films need to be controlled. In the previous work of our group, using multi-line

beam (MLB) CLC, (211)-(110)-(111) oriented poly-Si thin films with 100 μm long grains were formed at a high laser exposure energy regime. We found that MLB-CLC is a promising technology to form preferentially oriented poly-Si thin films. Poly-Si TFTs with 450 $cm^2V^{-1}s^{-1}$ electron mobility were fabricated on these poly-Si films. For ultrahigh-mobility TFTs, (100)-dominantly oriented poly-Si thin films with large crystal grains have generated a high demand. In this work, utilizing the MLB-CLC, we focused on forming highly (100) oriented poly-Si thin films and fabricating ultrahigh-performance LTPS-TFTs on these films.

1.3 Dissertation overview

This dissertation consists of six chapters, as illustrated in Fig. 1.3. The purpose of our research is formation of highly (100)-oriented poly-Si thin films and fabrication of ultrahigh-performance LTPS-TFTs on these films. We studied in the mechanism of (100) poly-Si thin film formation and TFT's performance enhancement to develop these devices in practical applications.

Chapter 2 describes the MLB-CLC technology that was applied to form (100) poly-Si thin films and characterization of the (100) poly-Si thin films. Crystallinities of the poly-Si films are very important for device performance. Various measurement methods were applied to characterize the poly-Si thin films. It shows that the poly-Si thin films had an excellent orientation preference and (100) crystal grains of approximately 20 x 2 μm^2 were dominant in very large areas. These films are promising to realize excellent TFTs. (Main paper 3)

Chapter 3 describes the effect of crystallization conditions on the crystallinities of the poly-Si thin films. The crystallization conditions play a decisive role for the orientation of the film. The conditions of overlapping ratio, scanning speed, and laser power were varied to investigate their effect on the crystallinities. These results suggest the mechanism of (100) texture formation and development of (100) orientation in large areas of the films. (Main papers 3)

Chapter 4 shows the fabrication process and characterization of LTPS-TFTs fabricated on (100) poly-Si thin film. With a low temperature process of under 550°C, ultrahigh performance TFTs were achieved. They have ultrahigh-mobility of 1010 cm^2V^-

$^{1}s^{-1}$ and excellent threshold voltage, sub-threshold slope, and ON/OFF ratio. Variation of TFTs' performance was also described. Characteristics of PMOS-TFTs were also described in this chapter. (Main paper 1, 2)

Chapter 5 shows discussions in the mechanism of (100) texture formation, orientation preference development in large areas, and TFT's performance enhancement. These discussions are based on our above results. The mechanism is very important for developing this technology.

In chapter 6, we conclude the achievements of this research. In addition, we suggest some works to develop this technology in the future.

References

[1] P. G. LeComber, W. E. Spear, and A. Ghaith, "*Amorphous-silicon field-effect device and possible application,*" Elec. Lett. **15**, 179 (1979).

[2] K. Nomura, H. Ohta, A. Takagi, T. Kamiya, M. Hirano, and H. Hosono, "*Room-temperature fabrication of transparent flexible thin-film transistors using amorphous oxide semiconductors,"* Nature **432**, 488 (2004).

[3] H. Yabuta, M. Sano, K. Abe, T. Aiba, T. Den, H. Kumoni, K. Nomura, T. Kamiya, and H. Hosono, "*High-performance thin-film transistor with amorphous InGaZnO4 channel fabricated by room temperature rf-magnetron sputtering,*" Appl. Phys. Lett. **89**, 112123 (2006).

[4] H-C. Cheng, C-C. Tsai, J-H. Lu, H-H. Chen, B-T. Chen, T-K. Chang, and C-W. Lin, "*Periodically Lateral Silicon Grains Fabricated by Excimer Laser Irradiation with a-Si Spacers for LTPS TFTs,*" J. Electrochem. Soc. **154**(1), J5 (2007).

[5] G. Fotunato, L. Mariucci, R. Carluccio, A. Pecora, V. Forglietti, "*Excimer laser crystallization techniques for polysilicon TFTs,*" Appl. Surf. Sci. **154**, 95 (2000).

[6] C. Tao, R. Ishihara, W. Mestselaar, K. Beenakker, and M-Y. Wu, "*Location and Crystallographic Orientation Control of Si Grains through Combined Metal Induced Lateral Crystalization and μ-Czochralski Process,*" Jpn. J. Appl. Phys. **47**, 1880 (2008).

[7] W-K. Lee, S-M. Han, J. Choi, M-K. Han, "*The characteristics of solid phase crystallized (SPC) polycrystalline silicon thin film transistors employing amorphous silicon process,*" J. Non-Crys. Solids **354**, 2509 (2008).

[9] L. Michalas, M. Koutsoureli, G.J. Papaioannou, D.N. Kouvatsos, A.T. Voutsas, "*Hydrogen passivation on Sequential Lateral Solidified poly-Si TFTs,*" Mircroelectronic Engineering **90**, 72 (2012).

[10] S. Morisaki, S. Hayashi, Y. Fujita, S. Higashi, "*Improvement in Characteristic Variability of TFTs Using Grain Growth Control by Micro Thermal Plasma Jet Irradiation on a-Si Strips,*" J. Display Tech. **10**, 950 (2014).

[11] A. Hara, M. Takei, F. Takeuchi, K. Suga, K. Yoshino, M. Chida, T. Kakehi, Y. Ebiko, Y. Sano, and N. Sasaki, "*High-Performance Polycrystalline Silicon Thin Film Transistors on Non-Alkali Glass Produced Using Continuous-Wave Laser Lateral Crystallization,*" Jpn. J. Appl. Phys. **43**, 1269 (2004).

[12] C-H Chou, W-S Chan, I-C Lee, C-L. Wang, C-Y Wu, P-Y. Yang, C-Y. Liao, K-Y. Wang, and H-C Cheng, "*High-Performance Single-Crystal-Like Strained-Silicon Nanowire Thin-Film Transistors via Continuous-Wave Laser Crystallization,*" IEEE Electron Device Lett., **36**, 348 (2015).

[13] T. Satô, Y. Takeishi, and H. Hara, "*Effects of Crystallographic Orientation on Mobility, Surface State Density, and Noise in p-Type Inversion Layers on Oxidized Silicon Surfaces,*" Jpn. J. Appl. Phys., **8**(5), 588 (1969).

[14] T. Satô, Y. Takeishi, and H. Hara, "*Mobility Anisotropy of Electrons in Inversion Layers on Oxidized Silicon Surfaces,*" Phys. Rev. B, **4**(6), 1950(1971).

[15] S.-I. Takagi, A. Toriumi, M. Iwase, and H. Tango, "*On the Universality of Inversion Layer Mobility in Si MOSFET's: Part II - Effects of Surface Orientation,*" IEEE Trans. Elec. Devices **41**, 2363 (1994).

[16] D. Colman, R. T. Bate, and J. P. Mize, "*Mobility Anisotropy and Piezoresistance in Silicon p-Type Inversion Layers,*" J. Appl. Phys., **39**(4), 1968.

[17] F. F. Fang and A. B. Fowller, "*Transport Properties of Electrons in Inverted Silicon Surfaces*", Phys. Rev., 169(3), 619(1968).

[18] Y. Miura, "*Effect of Orientation on Surface Charge Density at Silicon-Silicon Dioxide Interface,*" Jpn. J. Appl. Phys., **4**, 598 (1965).

[19] E. Arnold and G. Abowitz, "*Effect of Surface States on Electron Mobility in Silicon Surface-Inversion Layers,*" Appl. Phys. Lett., **9**(9), 344(1966).

[20] G. Abowitz, E. Arnold, and J. Ladell, "*Symmetry of Interface Charge Distribution in Thermally Oxidized Silicon,*" Phys. Rev. Lett., **18**(14), 543(1967).

[21] S.-I. Takagi, A. Toriumi, M. Iwase, and H. Tango, "*On the Universality of Inversion Layer Mobility in Si MOSFET's: Part I - Effects of Substrate Impurity Concentration,*" IEEE Trans. Elec. Devices **41**, 2347 (1994).

[22] J. Levinson, F. R. Shepherd, P. J. Scanlon, W. D. Westwood, G. Este, and M. Rider, "*Conductivity behavior in polycrystalline semiconductor thin film transistors,*" J. Appl. Phys. **53**(2), 1193(1982).

[23] J. Bardeen and W. Shockley, "*Deformation Potentials and Mobilities in Non-Polar Crystals,*" Phys. Rev. **80**(1), 72(1950).

[24] S-I. Takagi, J. L. Hoyt, J. J. Welser, and J. F. Gibbons, "*Comparative study of phonon-limited mobility of two-dimensional electrons in strained and unstrained Si metal-oxide-semiconductor field-effect transistors,"* J. Appl. Phys. 80(3), 1567(1996).

[25] G. Sun, Y. Sun, T. Nishida, and S. E. Thompson, "*Hole mobility in silicon inversion layers: Stress and surface orientation,*" J. Appl. Phys. 102, 084501(2007).

[26] M. O. Baykan, S. E. Thompson, and T. Nishida, "*Strain effects on three-dimensional, two-dimensional, and one-dimensional silicon logic devices: Predicting the future of strained silicon,*" J. Appl. Phys. 108, 093716 (2010).

[27] J. Welser, J. L. Hoyt, J. F. Gibbons, "*NMOS and PMOS Transistors Fabricated in Strained Silicon/Relaxed Silicon-Germanium structures,*" IEDM Tech. Dig., 1000 (1992).

[28] T. Tezuka, N. Sugiyama, T. Mizuno, and S-I. Takagi, "*High-performance Strained Si-on-Insulator MOSFETs by Novel Fabrication Processes Utilizing Ge-Condensation Technique,*" Symp. VLSI Tech. Dig., 96 (2002).

[29] K. Rim, S. Narasimha, M. Longstreet, A. Mocuta, and J. Cai, "*Low Field Mobility Characteristics of Sub-100 nm Unstrained and Strained MOSFETs,*" IEDM Tech. Dig., 43 (2002).

Chapter 2: (100)-dominantly Oriented Poly-Si Thin Film Formation with Multiline Beam Continuous-wave Laser Lateral Crystallization

2.1 Introduction

Formation of (100) oriented poly-Si thin films have been attracted much attention to enhance the performance of LTPS-TFTs because (100) crystals provide the highest electron mobility. With conventional ELA and CLC technologies, a (100) poly-Si thin film has been a challenging issue to researchers [1-6]. By combining the ELA with additional processes such as metal induced lateral crystallization (MILC) and μ-Czochralski, well crystal-oriented poly-Si thin films were formed and high-performance TFTs with 998 $cm^2V^{-1}s^{-1}$ electron mobility have been reported [7-10]. However, this method is applicable only to the substrate with a structure of SiO_2/Si and the SiO_2 patterning is needed. By using CLC, the poly-Si thin films have advantages that are large crystal grain size and dimensional crystal growth. Therefore, the effect of grain boundaries on TFT's performance is significantly reduced [11,2]. Formation of preferentially oriented poly-Si thin films with CLC becomes crucial. Especially, (100) oriented poly-Si thin films are the most important. In the previous work of our group, we have deformed the Gaussian laser beam into multi-line beam (MLB) by combining CLC with a diffractive beam homogenizer and an optics to improve laser energy distribution. Therefore, the energy density of laser beams is relatively uniform along the width direction of the beam. Uniform poly-Si thin films can be obtained by using MLB-CLC. In fact, highly bi-axial oriented poly-Si thin films were formed by MLB-CLC at a high laser exposure energy level (9 W laser power and 0.1 cm/s scanning speed). At this condition, long (211)-(110)-(111) crystals were dominant in the film [13-14]. MLB-CLC is a promising technology to make the poly-Si thin films uniformly oriented. Up to now, controlling poly-Si thin films oriented at (100) plane is highly demanded for high electron mobility. In this work, we form highly (100) oriented poly-Si thin films with MLB-CLC and precisely characterized crystallinities of the poly-Si films. Moreover, we developed (100) textures in large areas with an overlapping scanning.

2.2 Experimental

2.2.1 Sample preparation

Amorphous Si (a-Si) samples were prepared as follows. An a-Si film of 150 nm thickness deposited at a temperature of 430 ^{o}C by Plasma-Enhanced Chemical Vapor Deposition (PECVD) on a 1 μm thick SiO_2 buffer of a quartz substrate with an OH concentration of below 100 ppm. The thickness of the a-Si was determined by penetration length of laser source with wavelength of 532 nm. Then, a cap SiO_2 of 100 nm thickness were deposited by the PECVD to reduce surface roughness of the film [15]. To reduce the large amount of hydrogen, the film was partially dehydrogenated by furnace annealing at 490 ^{o}C in N_2 ambient for an hour.

2.2.2 Application of multiline beam continuous-wave laser lateral crystallization

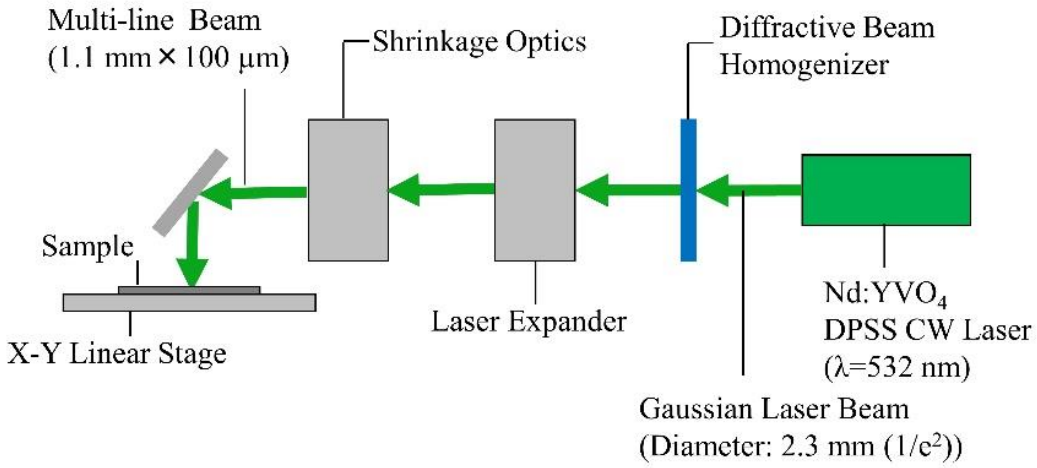

Fig. 2.1 Schematic of MLB-CLC system.

The schematic of MLB-CLC system is shown in Fig. 2.1. We used 532 nm continuous-wave (CW) laser of diode pump solid state (DPSS). The original laser beam has circular shape of 2.3 mm diameter and Gaussian energy distribution. After passing through the diffractive beam homogenizer and the optics, Gaussian beam is deformed into multiline

parallel beam. The number of line beam and energy distribution between line beams can be changed by adjusting the position of homogenizer and optics.

The top-view and cross-sectional profiles of multiline laser beam are shown in Figs. 2.2(a)-2.2(c). The laser beam have three line beams and approximately 1100 μm width. The energy density of each line beam is relatively uniform along beam width. The intensity of the center line beam is smaller and more uniform than that of others. By using MLB-CLC, preferentially oriented poly-Si thin films can be formed because crystal nucleation can occur at the exposed regions between line beams. These regions have approximately uniform supercooling temperature; therefore, preferentially oriented crystal nuclei can be grown. For laser crystallization, as the X-Y stage with samples move along X axis, they would be irradiated with the laser.

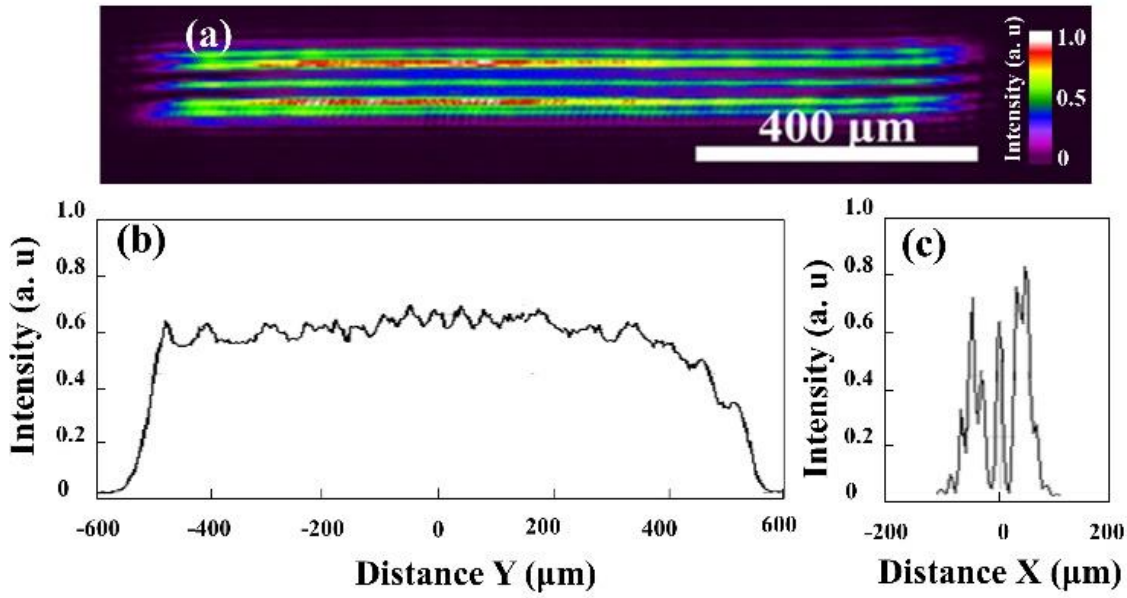

Fig. 2.2 (a) Top-view, (b) Y-cross-sectional, and (c) X-cross-sectional profiles of multi-line laser beam [17].

2.2.3 Overlapping scanning process

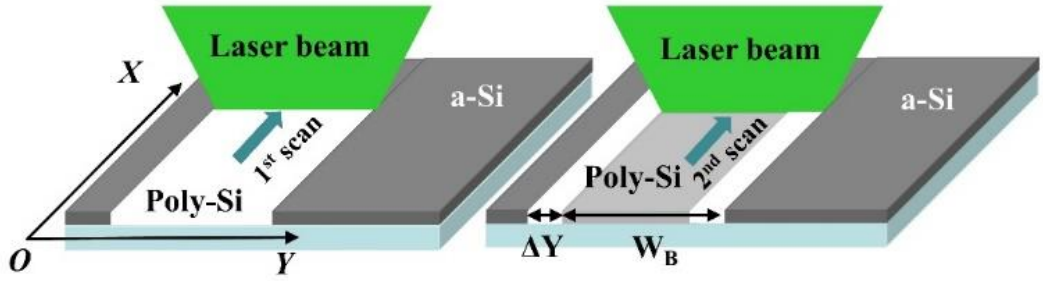

Fig. 2.3 Schematic of scanning process [17].

The laser beam was scanned over the samples with single scans and overlapped scans. The schematic of scanning process is shown in Fig. 2.3. The sample was placed on an X-Y stage. It was irradiated by the laser beams as the stage moved along X direction. After each linear single motion along *X*-axis, the stage shifted with a step of ΔY on *Y*-axis. Overlapping ratio (R_O) is determined as the ratio overlapped area between two continuous scans as follows:

$$R_O = \frac{W_B - \Delta Y}{W_B}, \tag{2.1}$$

where R_O is overlapping ratio, W_B is the width of laser beam.

Laser exposure energy per unit area can be averaged by overlapping scanning in the entire film.

After the a-Si thin films had been irradiated by the laser, the crystallization state of the films was observed by photomicroscope. Before the crystallinities of poly-Si films were characterized by X-ray diffraction (XRD), electron back scattering diffraction (EBSD), and 2-dimensional (2D) XRD, the SiO_2 cap layer had been removed by a buffered hydrofluoric acid (BHF) solution.

2.3 Results and discussions

2.3.1 (100) texture formation with MLB-CLC by single scans

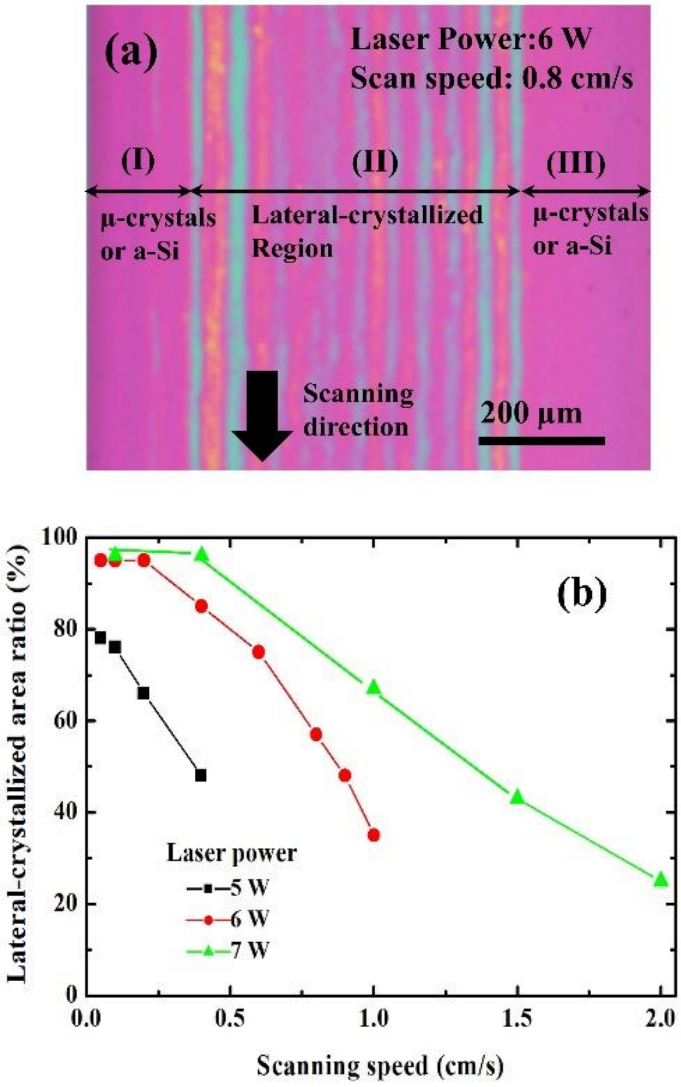

Fig. 2.4 (a) Microphotograph of a typical MLB-CLC poly-Si thin film formed at 6 W laser power and 0.8 cm/s scanning speed, (b) lateral-crystallized Si area ratio versus laser power and scanning speed [17].

Figure 2.4(a) shows the microphotograph of a poly-Si film formed by MLB-CLC at 6 W laser power and 0.8 cm/s scanning speed of a single scan. A lateral-crystallized Si area was observed at the middle of an irradiated region shown in the (II) area of Fig. 2.4(a). At the sides, the film typically consisted of microcrystals and a-Si regions observed in the

(I) and (III) regions. The lateral-crystallized area ratio dependence on the scanning speed and laser power is shown in Fig. 2.4(b). It shows that the Si could not be laterally crystallized above the condition of 0.4 cm/s speed for 5 W power, 1.0 cm/s for 6 W power, and 2.0 cm/s for 7 W power. These conditions are considered as a threshold for lateral-crystallized Si. Under the threshold of the scanning speed, the lateral-crystallized Si region became larger. And, approximately 100% area of the lateral-crystallized Si was definitely obtained at the speed of 0.2 cm/s for 6 W and 0.5 cm/s for 7 W.

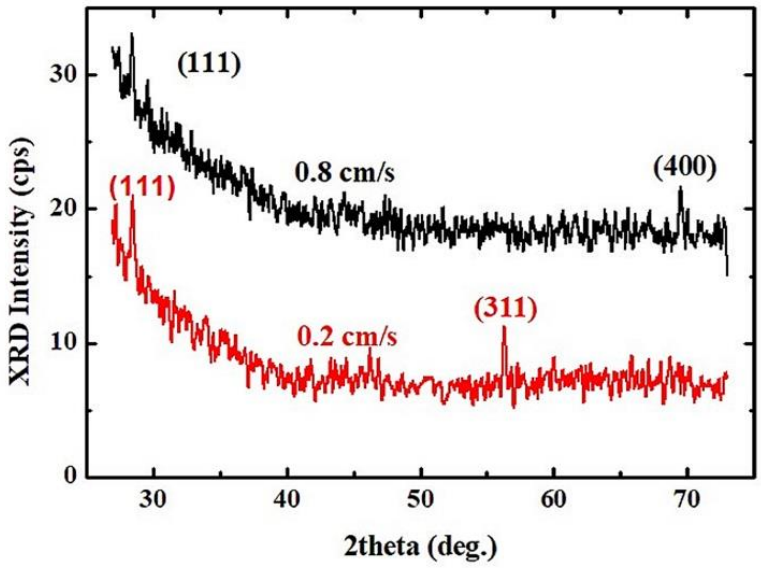

Fig. 2.5 Out-of-plane XRD spectra of MLB-CLC poly-Si films formed by single scans [17].

Figure 2.5 shows out-of-plane XRD spectra of the poly-Si films formed by single scans at two different conditions of the scanning speed of 0.8 and 0.2 cm/s with a fixed 6 W laser power. (400) and (111) peaks were observed at the former condition. Large (311) and (111) peaks were observed at the later in which the lateral-crystallized Si almost occupied the entire film. It indicated that the crystal orientation of the poly-Si film was strongly affected by the scanning speed of under the threshold. The preferential surface orientation of the poly-Si film turned from (100) to (311) as the speed decreased from the threshold.

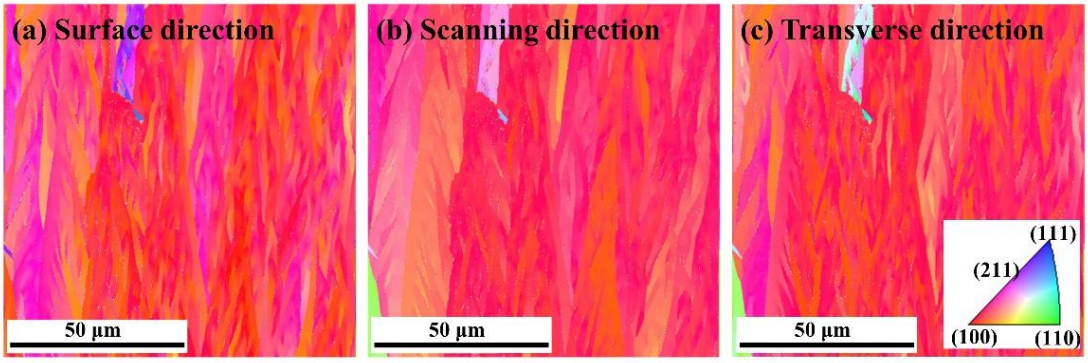

Fig. 2.6 Grain mappings of the poly-Si film measured by EBSD in (a) the normal surface direction, (c) laser scanning direction, and (c) tranverse direction (crystallization conditions: 6 W laser power and 0.8 cm/s scanning speed) [17].

Figures 2.6(a), 2.6(b), and 2.6(c) show the grain mappings of the poly-Si film measured by EBSD in the normal surface direction, scanning direction, and transverse direction, respectively. The pattern resolution of this measurement was 200 nm in a 100 × 100 μm^2 with 249000 points. The color chart is shown in the lower right corner of Fig. 2.6(c) and the red corresponds to (100) orientation. The crystallization conditions are 6 W laser power and 0.8 cm/s scanning speed as shown in the Fig. 2.4(a). The measurement was carried out at the lateral-crystallized area. Si crystal grains with an average size of 20 × 2 μm^2 were continuously developed along the laser scanning direction. The poly-Si film not only had a strong (100) orientation preference in the all three directions, but its crystallinity was also relatively uniform in the lateral-crystallized Si region. These (100) biaxial oriented crystals would significantly enhance the TFTs' performance.

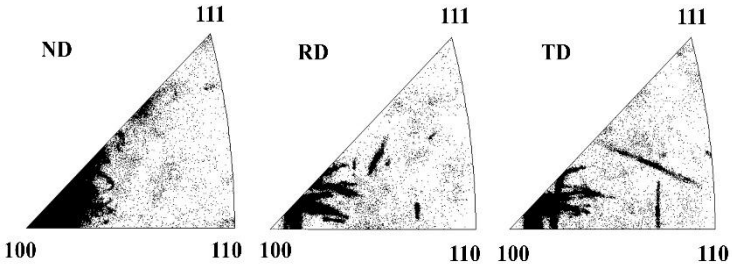

Fig. 2.7 Inverse pole figures of the poly-Si thin film in normal surface, scanning, and transverse directions, respectively.

EBSD inverse pole figures of the poly-Si thin film are shown in Fig. 2.7. The black dots in these figures correspond to the orientation of measured points. It appears that the orientations near (100) plane were dominant in all three figures. Note here that crystallization condition for the above (100) dominant orientation was 6 W laser power and 0.8 cm/s scanning speed. This condition was just above the threshold for lateral-crystallized Si.

2.3.2 Formation of (100) oriented large poly-Si thin films with overlapping scanning

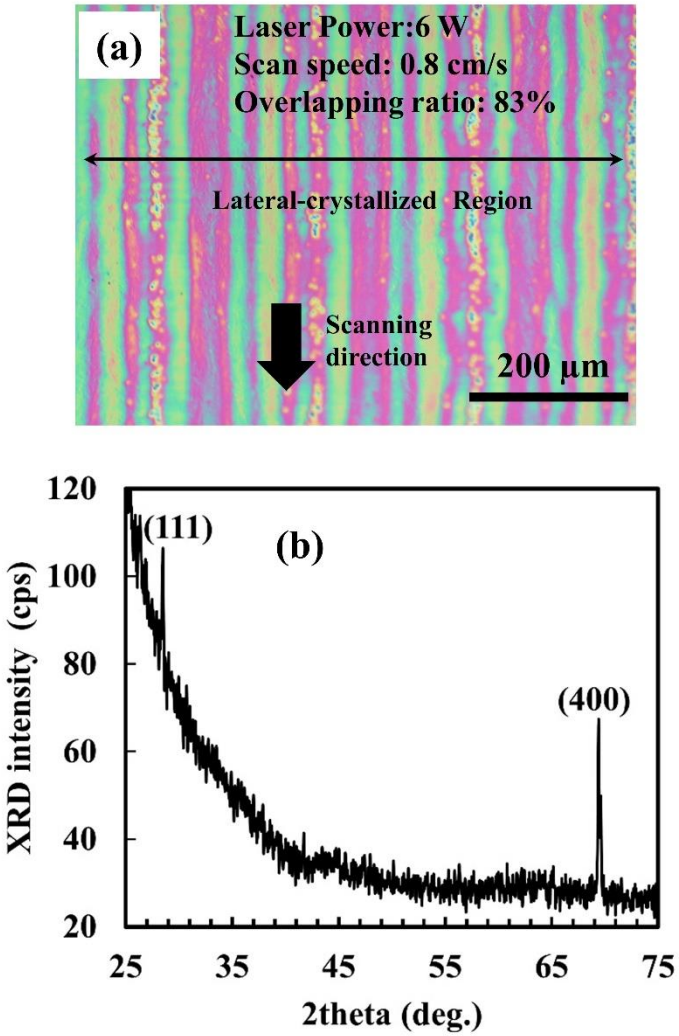

Fig. 2.8 (a) Microphotograph and (b) XRD spectra of a typical poly-Si film formed with overlapping scanning.

At the condition of (100) texture formation, approximately 50% of irradiated area could not be lateral-crystallized. For forming large (100) poly-Si thin film, overlapping scanning was applied. The photomicrograph of a poly-Si thin film formed with overlapping scanning is shown in Fig. 2.8(a). It indicates that the microcrystal regions disappeared and the lateral-crystallized Si area was enlarged in the whole film with overlapping. Figure 2.8(b) shows crystallility of laser crystallized poly-Si thin film measured by X-ray diffraction (XRD) measurement. This graph indicates that (111) and (400) peaks were observed. The XRD intensity of (400) peak was much higher than that of (111) one. According to XRD intensity ratio normalized by the silicon NBS standard reference material, the normalized XRD area intensity ratio of (400) peak reached up to 97.2% [16].

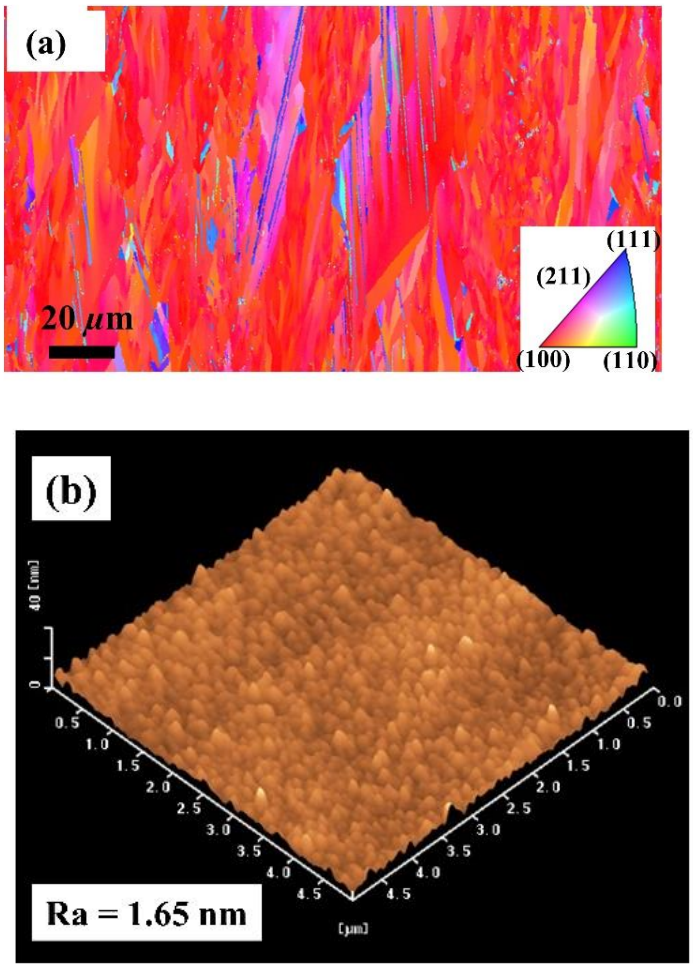

Fig. 2.9 (a) Grain map of surface direction and (b) surface morphology of the laser-crystallized poly-Si thin film (laser power: 6W, scanning speed: 0.8 cm/s, 83% overlapping ratio) [18].

Figures 2.9(a), and 2.9(b) show the grain mappings and the surface morphology of MLB-CLC poly-Si film measured by EBSD in the normal surface direction, and atomic force microscope (AFM), respectively. The conditions of the laser scanning were 6 W laser power, 0.8 cm/s scanning speed, and 83% overlapping ratio corresponding to appropriately six scans. The measurements were carried out in a 200 × 100 μm^2 area. Si crystal grains with an average size of 20 × 2 μm^2 were developed along the laser scanning direction. Furthermore, the poly-Si film had a strong (100) surface orientation preference. An average roughness (R_a) of 1.65 nm was found due to the cap SiO_2. It is found that the average roughness of the poly-Si film was relatively stable.

Two-dimensional orientation in a large area of the poly-Si thin film were measured by 2D-XRD. X-rays came to samples placed on the stage. The stage was rotated around the normal direction with rotation angle shift of 0.4°. Diffractive X-rays were detected by a 2D-detector. Diffraction images were collected twice per second. Schematic and photo of 2D-XRD equipment are shown in Fig. 2.10.

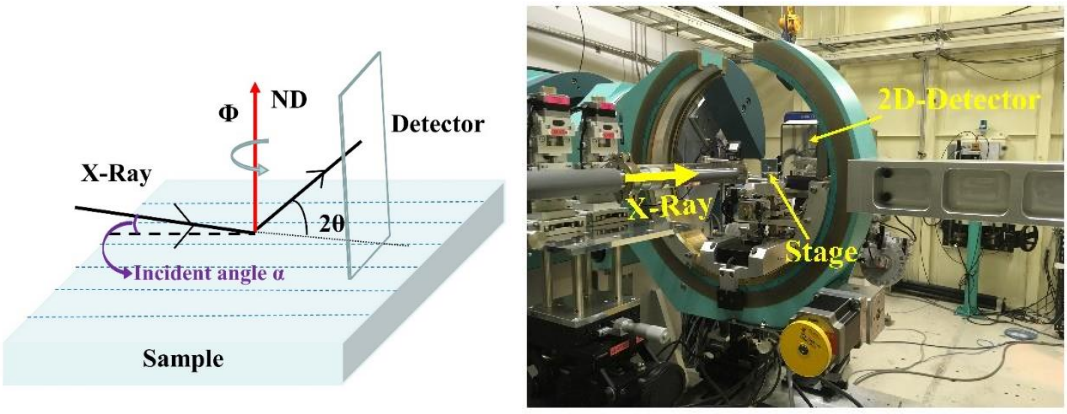

Fig. 2.10 (a) Schematic of 2D-XRD measurement, (b) photo of 2D-XRD apparatus.

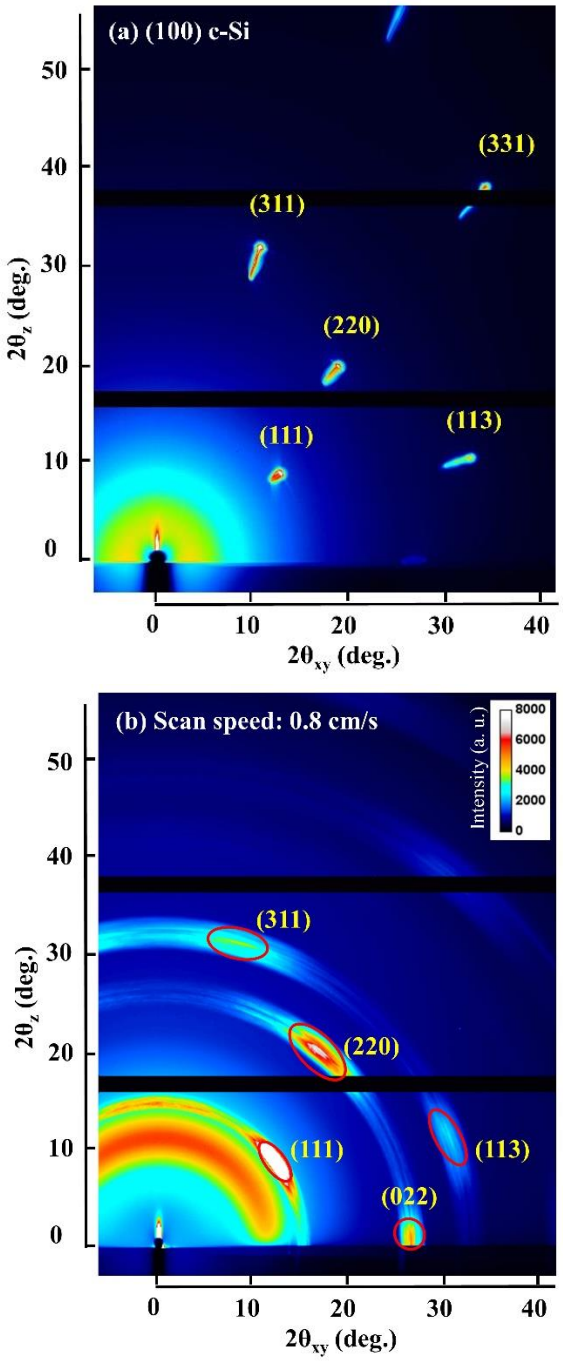

Fig. 2.11 2D-XRD images of (a) (100) c-Si and (b) the laser-crystallized poly-Si thin film (6 W laser power, 0.9 cm/s scanning speed, 83% overlapping ratio).

Figures 2.11(a), 2.11(b) show 2-Dimension (2-D) XRD images of the (100)Si single crystal wafer (c-Si) and poly-Si thin film, respectively. Crystallization conditions were 6 W laser power, 0.9 cm/s scanning speed, and 83% overlapping ratio. The vertical and horizontal axes of the images correspond to out-of-plane and in-of-plane directions,

respectively. The grazing angles of incident X-ray were 0.12° for the poly-Si film and 2° for the c-Si, respectively. The color chart corresponding to relative XRD intensity was shown in Fig. 5(b). Red rings observed at the 2theta of 14° in the 2-D XRD result of the poly-Si films was inelastic X-Ray scattering from quartz substrate. Peaks observed in the poly-Si films including (111), (220), (311), and (113) peaks were located as the same as those of the c-Si. The (022) one could not be observed in the image of the c-Si due to a large grazing angle. This result shows that the (100) surface orientation preference of the poly-Si thin film was extremely strong and comparable to (100) c-Si.

2.3.3 Biaxial tensile strain of poly-Si thin film

It has been reported that poly-Si thin films have high tensile strain that remarkably improves both electron and hole mobility. The strain of the poly-Si film is produced by the difference between the coefficient of silicon and the SiO_2 buffer layer, when the Si is heated beyond its melting point, and contracts during cooling relative to the SiO_2 buffer layer [17,18]. The strain and structural distribution of the (100) poly-Si thin films were characterized by Raman spectroscope comparing with the XRD.

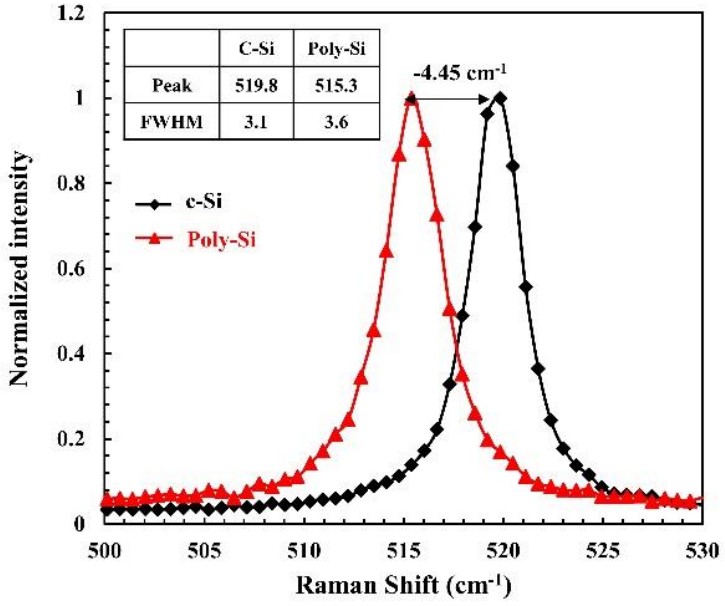

Fig. 2.12 Raman spectra of the poly-Si thin film and c-Si [17]

Figure 2.12 shows the micro-Raman spectra of the MLB-CLC poly-Si thin film and the single-crystal Si (c-Si) wafer. The full width at half maximum (FWHM) of the Raman peak of the poly-Si film was determined approximately that of the c-Si. This result demonstrated an excellent structural order of crystalline Si. In addition, the Raman peak of the poly-Si film were shifted $\Delta\omega$ = -4.45 cm^{-1} lower than that of the c-Si. A averaged thermal bi-axial tensile stress of 1112 MPa in the poly-Si was calculated by the relation equation of $\Delta\omega$ and stress (σ) [19,20]:

$$\sigma(\text{GPa}) = -0.25\ (\text{Gpa/cm}^{-1}) \times \Delta\omega\ (\text{cm}^{-1}) \tag{2.2}$$

From XRD spectrum of the poly-Si thin film shown in Fig. 2.8(b), two adjacent (400) peaks with various XRD intensities were observed at an angle (2θ) of 69.455° and 69.679°. These angles corresponding to characteristic X-Ray of Cu$K\alpha$(1) and Cu$K\alpha$(2) were shifted to a higher angle than that of standard Si. The lattice constant, which was calculated from Bragg's law, was 5.409 Å and 0.022 Å smaller than the equilibrium lattice constant in the out-of-plane direction. This value indicates that the MLB-CLC poly-Si film had an out-of-plane compressive strain (ε_0) of -0.4%. That is in turn the consequence of a biaxial tensile strain. According to the published literature of M. T. Currie, et al [21], an electron mobility enhancement of approximately 45% can be achieved with this value of the biaxial tensile strain.

On the other hand, an average thermal explanation coefficient (α) of 4.67 x 10^{-6} K^{-1} was evaluated for the poly-Si thin films between room temperature and melting point (ΔT) as the following equation:

$$\alpha = \frac{\varepsilon_0}{2\upsilon\Delta T} \tag{2.3}$$

where υ = 0.279 is the Poisson constant of Si (100) in <001> direction and ε_0 is the biaxial tensile strain [17,22-26].

It is worth noticing here that the thermal expansion coefficient of the poly-Si is greater than that of single crystal Si of 3.8 x 10^{-6} K^{-1}, and is in good agreement with the suggestion of H. Tada et al [17].

2.4 Conclusions

We demonstrated (100) poly-Si thin films formed by using MLB-CLC with single scans. The crystallization conditions for (100) texture formation were just above a threshold for lateral crystallized Si. With these conditions, the poly-Si thin films had (100) orientation in all surface, scanning, and transverse directions. Si(100) crystal grains developed along the laser scanning direction. They were relatively uniform and had a very large size of 20 × 2 μm^2. However, approximately 50% area of the irradiated film could not be laterally crystallized with these conditions. By overlapping scanning, (100) textures were achieved in a large area of the film. Moreover, the poly-Si thin films had a high bi-axial tensile strain in planar direction and a compressive strain in depth direction. Average stress was determined as 1112 MPa. The crystallinities of the poly-Si films were characterized by 2-Dimension X-Ray diffraction. It is found that the poly-Si thin films had (100)-surface oriented crystals in large areas, dominantly. In summary, the MLB-CLC poly-Si thin films had excellent orientation preference, large crystal grain size, well structural order that was comparable to the c-Si, and had high bi-axial tensile strain. These excellent crystallinities are advantages and make MLB-CLC a promising technology to realize ultrahigh-performance TFTs with large substrates.

References

[1] J-Y Park, H-H Park, K-Y Lee and H-K Chung, "*Design of Sequential Lateral Solidification Crystallization Method for Low Temperature Poly-Si Thin Film Transistors,*" Jpn. J. of Appl. Phys. **43**, 1280 (2004).

[2] G. Fotunato, L. Mariucci, R. Carluccio, A. Pecora, V. Forglietti, "*Excimer laser crystallization techniques for polysilicon TFTs,*" Appl. Surf. Sci. **154**, 95 (2000).

[3] D. P. Gosain, A. Machida, T. Fujino, Y. Hitsuda, K. Nakano, and J. Sato, "*Formation of (100)-Textured Si Film Using an Excimer Laser on a Glass Substrate,*" Jpn. J. Appl. Phys. **42**, L135 (2003).

[4] S. Fujii, S. Kuroki, X. Zhu, M. Numata, K. Kotani, and T. Ito, "*Analysis of Continuous-Wave Laser Lateral Crystallized Polycrystalline Silicon Thin Films with Large Tensile Strain,*" Jpn. J. Appl. Phys. **47**, 3046 (2008).

[5] N. Matsuo, Y. Aya, T. Kanamori, T. Nouda, and T. Miyoshi, "*Study of Crystal Growth Mechanism for Poly-Si Film Prepared by Excimer Laser Annealing,*" Jpn. J. Appl. Phys. **39**, 351 (2000).

[6] S. D. Brotherton, D. J. Mcculloch, and J. P. Gowers, "*Influence of Excimer Laser Beam Shape on Poly-Si Crystallisation,*" Jpn. J. Appl. Phys. **43**, 5114 (2004).

[7] M. Mitani, T. Endo, Y. Taniguchi, T. Katou, S. Shimoto, T. Ohno, S. Tsuboi, T. Okada, K. Azuma, G. Kawachi, and M. Matsumura, "*Ultrahigh-Performance Polycrystalline Silicon Thin-Film Transistors on Excimer-Laser-Processed Pseudo-Single-Crystal Films,*" Jpn. J. Appl. Phys. **47**, 8707 (2008).

[8] C. Tao, R. Ishihara, W. Metselaar, K. Beenakker, and M-Y. Wu, "*Location and Crystallographic Orientation Control of Si Grains through Combined Metal Induced Lateral Crystalization and μ-Czochralski Process,*" Jpn. J. Appl. Phys. **47**, 1880 (2008).

[9] X. Zeng, H. Wang, X. Sun, J. Li, "*Electric field-enhanced metal-induced lateral crystallization and P-channel poly-Si TFTs fabricated by it,*" Microelectro. J. **39**, 1189 (2008).

[10] T. Chen, R. Ishihara, K. Beenakker, "*Location- and Orientation-Controlled (100) and (110) Single-Grain Si TFTs without Seed Substrate,*" IEEE Trans. Electron Devices **57**, 2348 (2010).

[11] J. Levinson, F. R. Shepherd, P. J. Scanlon, W. D. Westwood, G. Este, and M. Rider, "*Conductivity behavior in polycrystalline semiconductor thin film transistors,*" J. Appl. Phys. **53**, 1193 (1982).

[12] A. Hara, M. Takei, F. Takeuchi, K. Suga, K. Yoshino, M. Chida, T. Kakehi, Y. Ebiko, Y. Sano, and N. Sasaki, "*High-Performance Polycrystalline Silicon Thin Film Transistors on Non-Alkali Glass Produced Using ContinuousWave Laser Lateral Crystallization,*" Jpn. J. Appl. Phys. **43**, 1269 (2004).

[13] S. Kuroki, Y. Kawasaki, S. Fujii, K. Kotani, "*Seed-Free Fabrication of Highly Bi-Axially Oriented Poly-Si Thin Films by Continuous-Wave Laser Crystallization with Double-Line Beams,*" J. Electrochem. Soc. **158**, H924 (2011).

[14] M. Yamano, S. Kuroki, T. Sato, and K. Kotani, "*High-performance poly-Si thin film transistors with highly biaxially oriented poly-Si thin films using double line beam continuous-wave laser lateral crystallization,*" Jpn. J. Appl. Phys. **53**, 03CC02 (2014).

[15] S. Fujii, S. Kuroki, X. Zhu, M. Numata, K. Kotani, and T. Ito, *"Roughness Reduction in Polycrystalline Silicon Thin Films Formed by Continuous-Wave Laser Lateral Crystallization with Cap SiO_2 Thin Films,*" Jpn. J. Appl. Phys. **48**, 04C129 (2009).

[16] M. C. Morris, H. F. McMurdie, E. H. Evans, B. Paretzkin, H. S. Parker, and N. C. Panagiotopoulos, "*Standard X-ray Diffraction Powder Patterns*," Natl. Bur. Stand. (U.S) Monogr. **25**, 13, 35 (1976).

[17] T. T. Nguyen, M. Hiraiwa, T. Koganezawa, S. Yasuno, and S.-I. Kuroki, "*Formation of (100)-oriented large polycrystalline silicon thin films with multiline beam continuous-wave lateral crystallization*," Jpn. J. Appl. Phys. **57**(3), 031302-1-031302-6 (2018).

[18] T. T. Nguyen, M. Hiraiwa, and S.-I. Kuroki, "*Ultrahigh-performance (100)-oriented polycrystalline silicon thin-film transistors and their microscopic crystal structures*," Appl. Phys. Exp., **10**, 056501 (2017).

[19] H. Tada, A. Kumpel, R. E. Lathrop, J. B. Slanina, P. Nieva, P. Zavracky, I. N. Miaoulis, and P. Y. Wong, "*Thermal expansion coefficient of polycrystalline silicon and silicon dioxide thin films at high temperatures,*" J. Appl. Phys. **87**, 4189 (2000).

[20] H. Kahn, R. Ballarini, A. H. Heuer, "*Thermal Expansion of Low-pressure Chemical Vapor Deposition Polysilicon Films,*" J. Mater. Res. **17**, 1855 (2002).

[21] P. Lengsfeld, N. H. Nickel, Ch. Genzel, and W. Fuhs, "*Stress in undoped and doped laser crystallized poly-Si,*" J. Appl. Phys. **91**, 9128 (2002).

[22] C-H Chou, W-S Chan, I-C Lee, C-L. Wang, C-Y Wu, P-Y. Yang, C-Y. Liao, K-Y. Wang, and H-C Cheng, "*High-performance Single-Crystal-Like Strained-Silicon Nanowire Thin-Film Transistors via Continuous-Wave Laser Crystallization,*" IEEE Electron Device Lett., **36**, 348 (2015).

[23] M. T. Currie, C. W. Leitz, T. A. Langdo, G. Taraschi, E. A. Fitzgerald, and D. A. Antoniadis, "*Carrier mobilities and process stability of strained Si n- and p-MOSFETs in SiGe virtual substrates,*" J. Vac. Sci. Technol. B **19**, 2268 (2001).

[24] Y. Okada and Y. Tokumaru, "*Precise determination of lattice parameter and thermal expansion coefficient of silicon between 300 and 1500 K,*" J. Appl. Phys. **56**, 314 (1984).

[25] J. J. Wortman and R. A. Evans, "*Young's Modulus, Shear Modulus, and Poisson's Ratio in Silicon and Germanium,*" J. Appl. Phys. **36**, 153 (1965).

[26] W. A. Brantley, "*Calculated elastic constants for stress problems associated with semiconductor devices,*" J. Appl. Phys. **44**, 534 (1973).

Chapter 3: Effect of Crystallization Conditions on Crystallinities of Poly-Si Thin Films

3.1 Introduction

In chapter 2, biaxially (100)-oriented poly-Si thin films formed by MLB-CLC with single scans were discussed. The crystallization conditions of laser power and scanning speed for (100) texture formation were just above the threshold for lateral-crystallized Si. By overlapping scanning, (100) textures were achieved in large areas. The poly-Si thin films predominantly had (100) surface orientation. These films are promising to realize ultrahigh-performance TFTs that are the key for the progress of Si device technology. Ultrahigh-performance TFTs, which are comparable to c-Si devices, can be applied for digital processing in which c-Si wafers have mainly used. We found that the crystallinities of the poly-Si thin films were strongly dependent on crystallization conditions. Therefore, investigating the effect of crystallization conditions on the crystallinities of the poly-Si thin films becomes extremely essential for comprehending the mechanism of (100) orientation control, and developing this technology. The effect of crystallization conditions on the crystallinity of poly-Si thin films has been investigated for some kinds of crystallization methods [1-7]. After this investigation, the optimal crystallization conditions would be suggested for device fabrication. In this chapter, we investigate their effectible factors consisting of laser power, scanning speed, and overlapping ratio. These results would be very important for understanding the mechanism of (100) texture formation as well as optimizing the crystallization conditions.

3.2 Experimental

3.2.1 Investigation of laser beam configuration and overlapping scanning on crystallinities of poly-Si thin films

In the chapter 2, a (100)-surface-oriented poly-Si thin film was realized in a large area with 83% overlapping ratio. Its crystallinities were also characterized by EBSD. In this chapter, overlapping scanning dependence of crystallinities of poly-Si thin films would be clarified. In order to investigate the effect of the overlapping scanning on the crystallinities of poly-Si thin films, we based on the good conditions of laser power and scanning speed for forming (100) oriented poly-Si thin films by single scans.

Subsequently, these optimal conditions were fixed with 6 W laser power and 0.9 cm/s scanning speed. At these fixed conditions, the overlapping ratio was varied from 48% to 98%. The change of the overlapping ratio corresponding to the modification of the number of overlapped scans (from 2 to 45 scans). The crystallinities of these laser-crystallized poly-Si thin films were characterized by XRD and EBSD measurements after their cap SiO_2 layers were removed.

3.2.2 Investigation of scanning speed and laser power on crystallinities of poly-Si thin films

The laser power and scanning speed were varied to investigate their effects on the crystallinities of the poly-Si films. Firstly, as the overlapping ratio was fixed at 83% and laser power was fixed at 6 W, the scanning speed was changed from 0.2 to 1.0 cm/s. The surface orientation of the laser-crystallized poly-Si thin films was examined by out-of-plane XRD and 2D-XRD measurements. Secondly, the laser power was changed from 5 to 8 W and the scanning speed was also varied to find the appropriate conditions for forming (100) poly-Si thin film. The crystallinities of the poly-Si thin films were then characterized by the XRD and EBSD measurements.

3.3 Results and discussions

3.3.1 Effect of overlapping scanning on the crystallinities of poly-Si thin films

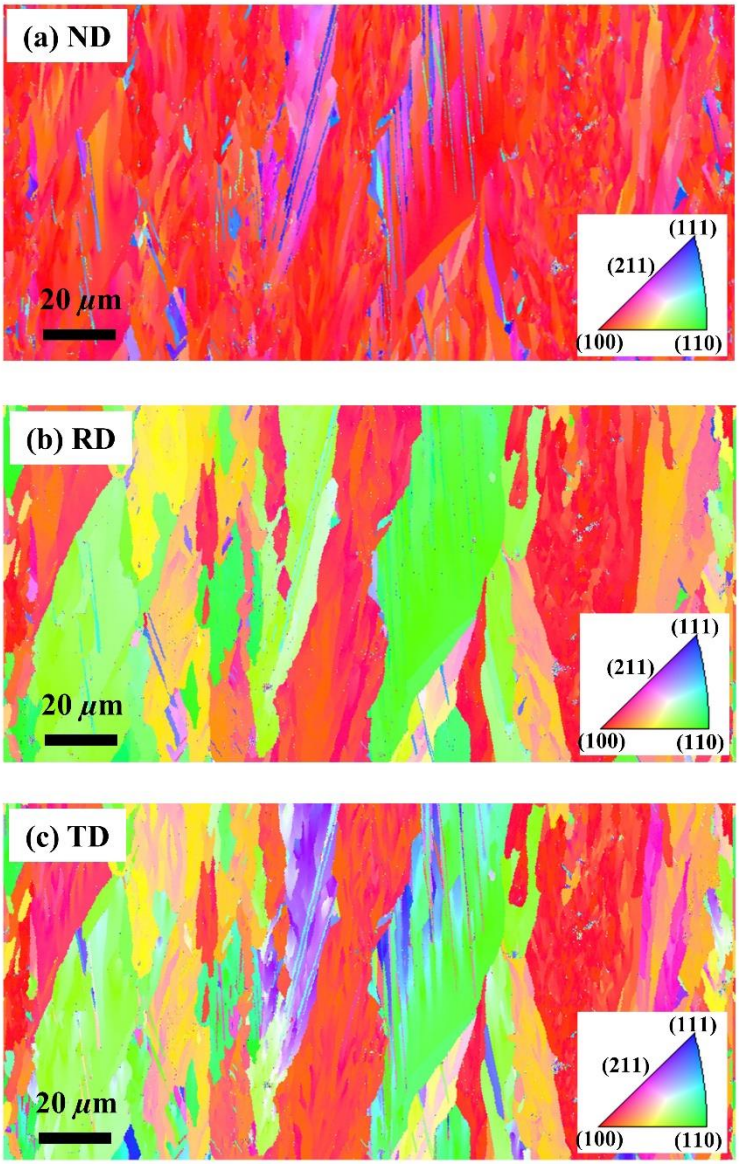

Fig. 3.2 Grain mapping of the MLB-CLC poly-Si film (6 W laser power, 0.8 cm/s scanning speed, 83% overlapping ratio)

Figures 3.2(a), 3.2(b) and 3.2(c) show grain mapping in the normal surface, scanning, and transverse directions, respectively, of the MLB-CLC poly-Si film formed with 83%

overlapping ratio. It is apparent that (100) orientation preference was stable in the normal surface direction. However, it was locally changed to (110) or other planes in the scanning and transverse directions. These crystals were rotated around [001] axis from (010) to (110) plane in laser scanning and from (100) to (110) plane in transverse direction.

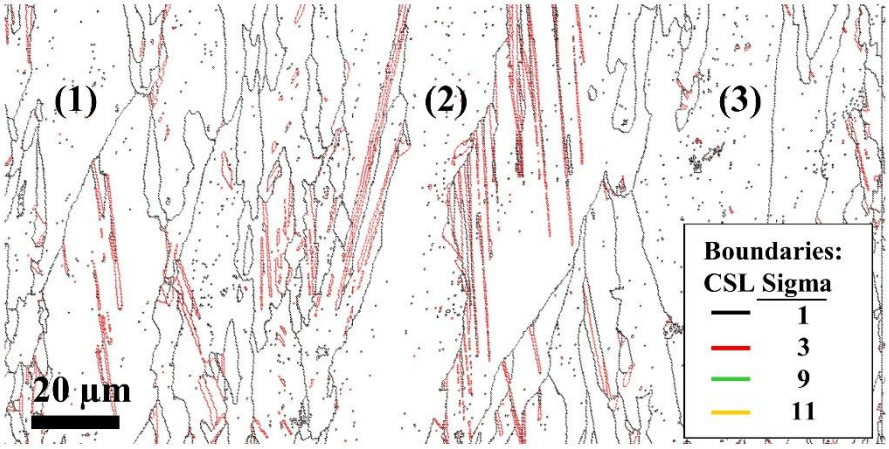

Fig. 3.3 Grain boundary map of the laser-crystallized poly-Si thin film (laser power: 6W, scanning speed: 0.8 cm/s, 83% overlapping ratio).

Figure 3.3 shows grain boundary mapping evaluated as coincidence site lattice (CSL) measured by EBSD**.** CSL Σ1 and Σ3 boundaries were typically observed. Σ1 is small angle grain boundary and Σ3 is crystal twin. Especially, the CSL grain boundaries were absent in very large areas of over 100 × 10 μm^2 as shown in (1), (2), and (3) of Fig. 3.3 because crystals were bi-axially oriented at (100) and they had small misorientation angles. These results indicate that although (100) orientation preference was unchanged in the normal surface direction, it was unstable in the scanning and transverse directions and then significantly changed characteristics of grain boundaries.

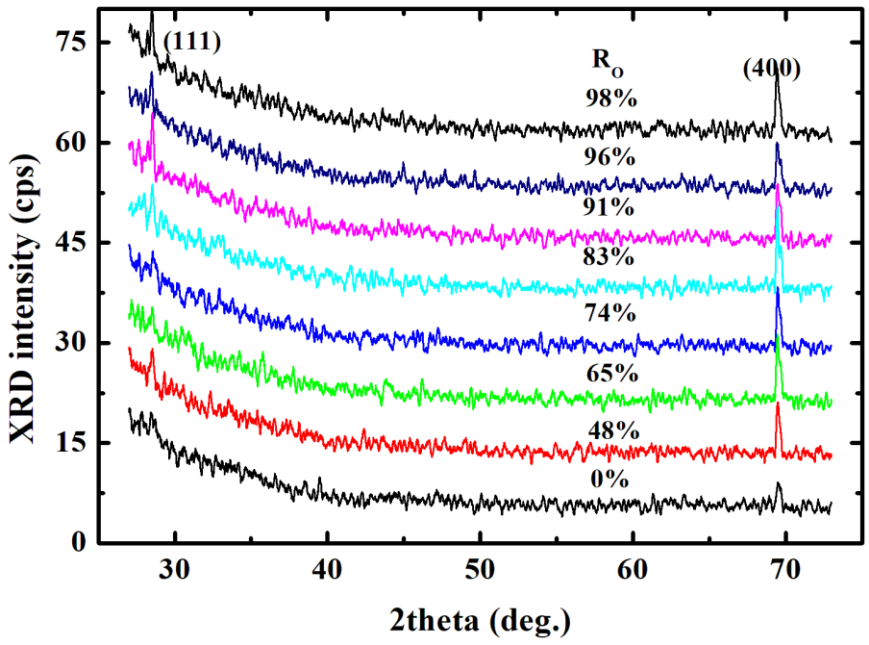

Fig 3.4 XRD spectra of the poly-Si films with various overlapping ratios (Laser power: 6 W, scanning speed: 0.9 cm/s) [8].

Figure 3.4 shows XRD spectra of the poly-Si films as the overlapping ratio was varied from 0% (single scan) to 98% at a fixed 0.9 cm/s scanning speed and 6 W laser power. It was found that small (400) and (111) peaks appeared at a single scan. The (400) peak became larger with the overlapping ratio increasing to 48% and then saturated at higher ratios. Note here that the lateral-crystallized Si regions occupied 48% area at a 0.9 cm/s single scan. Therefore, the lateral-crystallized region was smaller than the measured regions that probably include microcrystal region. And the lateral-crystallized poly-Si area became larger and occupying in the whole film by overlapping scanning, therefore the large (400) peaks were seen in the XRD spectra without another peak appearance.

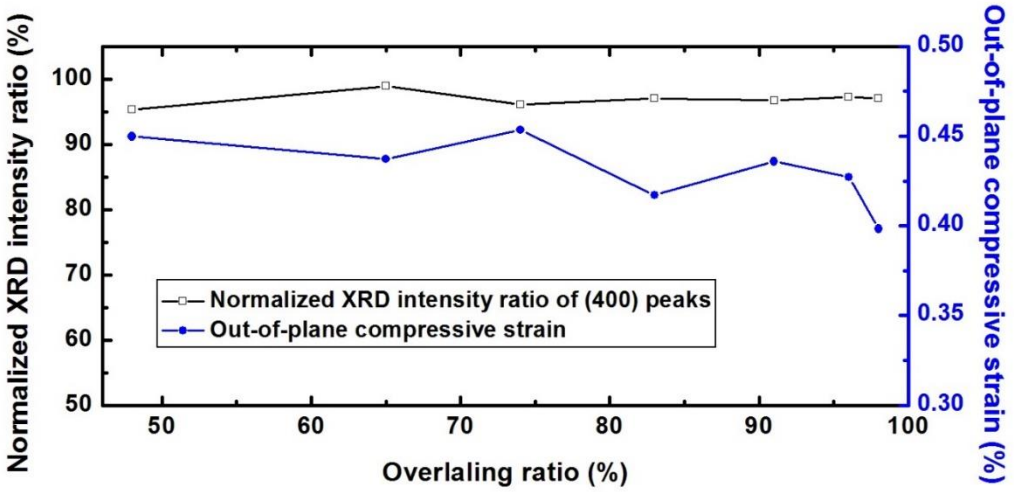

Fig. 3.5 Plots of normalized ratio of (400) peak and out-of-plane compressive strain of the poly-Si film versus the scanning speed values.

According to the silicon NBS standard reference material [9], volume ratios of the typical crystal orientations of the observed peaks including (400) and (111) were calculated. The normalized ratio of (400) peaks is described as a function of overlapping ratio as shown in Fig. 3.5. The ratio of (400) peaks took a maximal value of approximately 97% and was relatively saturated with the overlapping scanning. In addition, the values of lattice constant were calculated from the diffraction angles (2θ) of the (400) peaks (derivation of Bragg's law). These values were determined to be smaller than the equilibrium lattice constant and exhibited the out-of-plane compressive strain of the poly-Si films. The values of the out-of-plane compressive strain versus the scanning speed and the overlapping ratio are shown in Fig. 3.5. The strain was slightly fluctuated between 0.37% and 0.47% with the variation of the overlapping ratio.

3.3.2 Effect of laser power and scanning speed on the crystallinities of poly-Si thin films

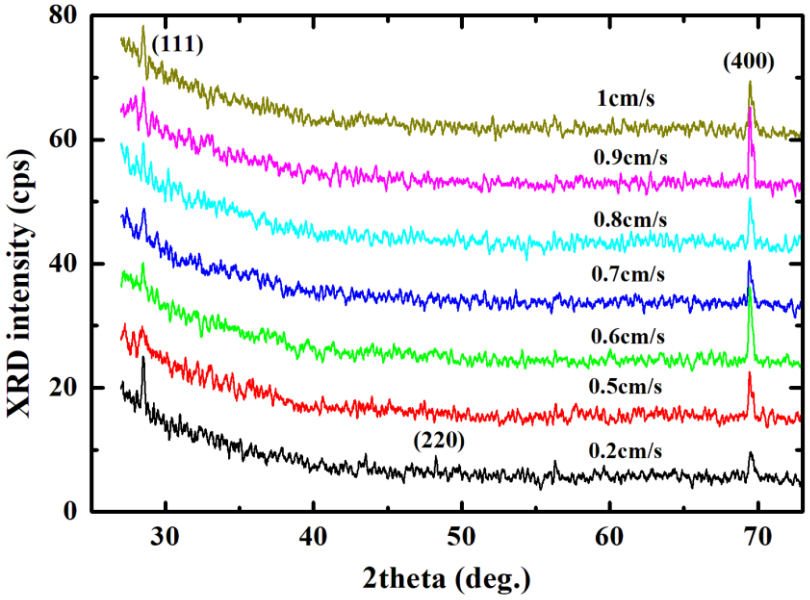

Fig. 3.6 XRD spectra of the poly-Si films with various conditions of scanning speed (Laser power: 6 W, overlapping ratio: 83 %) [8].

Figure 3.6 shows XRD spectra of the poly-Si thin films as the scanning speed varied from 0.2 to 1 cm/s with a fixed 6 W laser power and a fixed 83% overlapping ratio. It is found that the (111) and (400) peaks were typically observed at all conditions and the (400) peaks were much larger than the (111). The intensity of the (400) peaks was slightly fluctuated. Particularly, large (400) peaks appeared at the scan speed of 0.6 cm/s and 0.9 cm/s. They became smaller at other conditions. Especially at the 0.2 cm/s speed, the (111) peak became larger and the (400) peak contrastingly got smaller. The (311) peak observed at the single scan disappeared and a very small (220) peak appeared. At 1.0 cm/s, a smaller (400) peak was seen. The peaks disappeared at the speed of above 1 cm/s because the lateral-crystallized Si was inexistent.

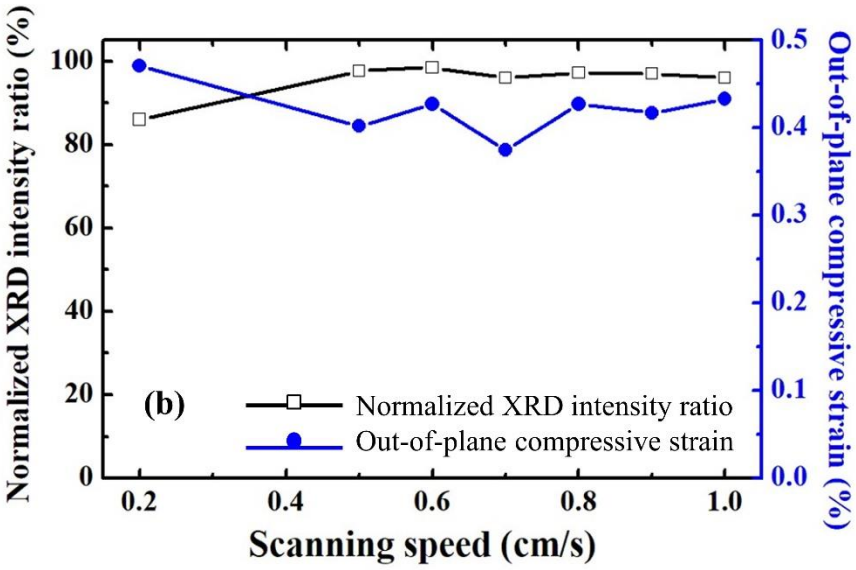

Fig 3.7 Plots of normalized ratio of (400) peak and out-of-plane compressive strain of the poly-Si film versus the scanning speed values [8].

Volume ratios of the typical crystal orientations of observed peaks including (400), and (111) were calculated. The normalized ratio of the (400) peaks is described as a function of the scanning speed shown in Fig. 3.7. A high ratio of up to 97% was obtained at the scanning speed of from 0.6 to 0.9 cm/s. As the scanning speed values decreased under 0.5 cm/s, this ratio was significantly reduced. At the scanning speed of 1.0 cm/s, the ratio was slightly reduced. Above 1.0 cm/s, the ratio could not be calculated because the peaks could not be observed. In addition, the values of lattice constant were calculated from the diffraction angles (2θ) of the (400) peaks (derivation of Bragg's law). These values were determined to be smaller than the equilibrium lattice constant and exhibited the out-of-plane compressive strain of the poly-Si films. The values of the out-of-plane strain versus the scanning speed are shown in Fig. 3.7. The strain was compressive, then these films had a compressive deformation in the depth direction. The strain was slightly fluctuated between 0.37% and 0.47% with the scanning speed.

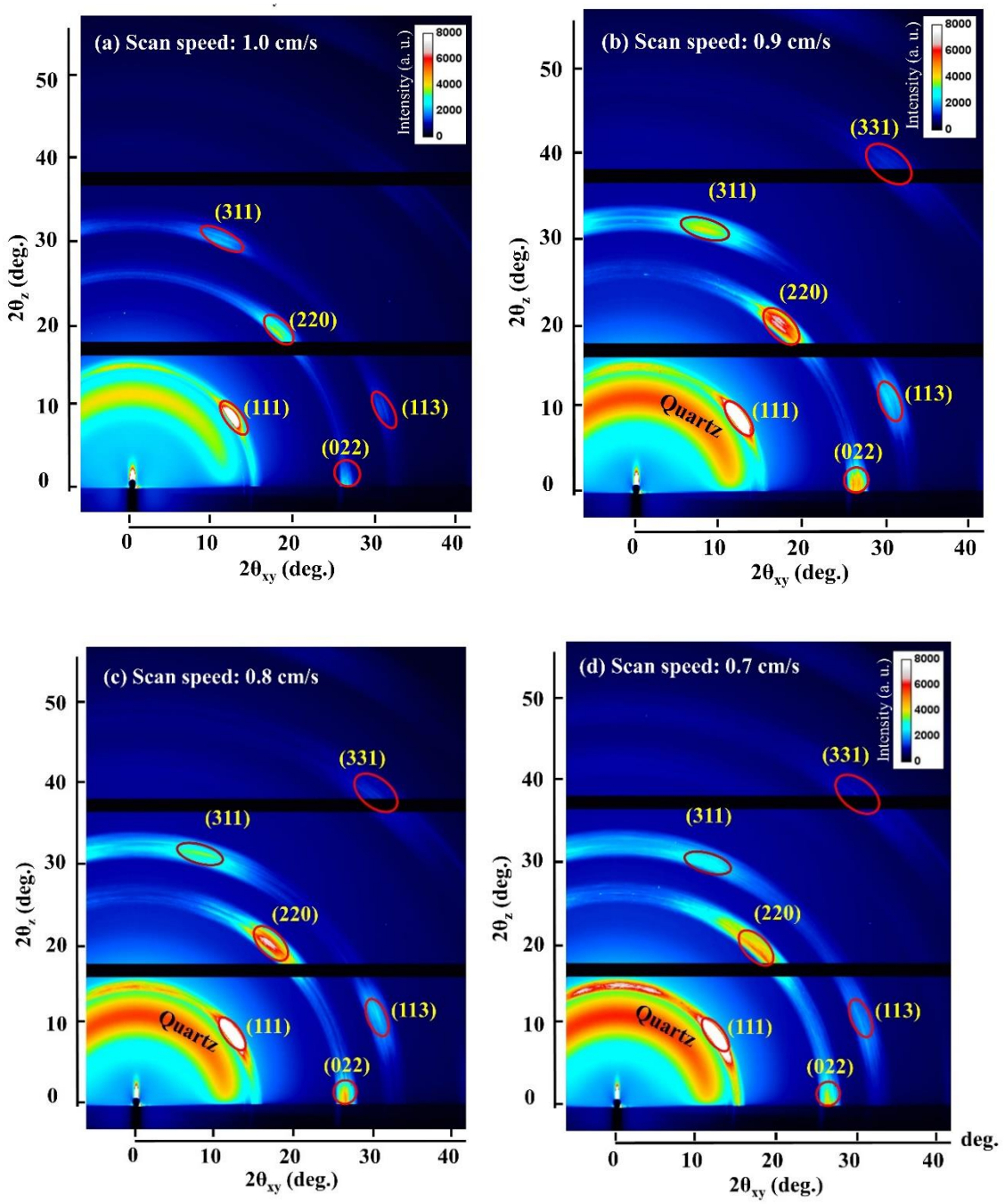

Fig. 3.8 2D-XRD images of (a) (100)Si single crystal and the poly-Si thin films at the scanning speed of (b) 1.0 cm/s, (c) 0.9 cm/s, and (d) 0.7 cm/s [8].

Figure 3.8 shows 2D- XRD images of the laser-crystallized poly-Si thin films. The conditions for the laser crystallization were fixed as the laser power of 6 W and overlapping ratio of 83%. The scanning speed was varied from 0.7 cm/s to 1.0 cm/s. The vertical and horizontal axes of the images correspond to out-of-plane ($2\theta_z$) and in-plane ($2\theta_{xy}$) directions, respectively. The grazing angles of incident X-ray were 0.12^o for the poly-Si films. These poly-Si films had similar bright peaks in 2D-XRD images including (111), (220), (022), (311), (113), and (331). They were similar to the peaks of (100) c-Si wafer. These results show that these poly-Si thin films had (100)-surface oriented crystals, dominantly. Moreover, these peaks expanded along Debye-Scherrer rings as the scanning speed decreased to 0.7 cm/s. This result shows that the crystals were partially rotated around (100) crystals as the scanning speed got slower. On the other hand, weak Debye-Scherrer rings with small peaks were observed at the scanning speed of 1 cm/s. As shown in Fig. 3.8(b), the lateral-crystallized Si was unclearly observed in this condition. It shows that polycrystalline phases were not dominant in this condition that can be considered as a threshold for lateral-crystallized Si.

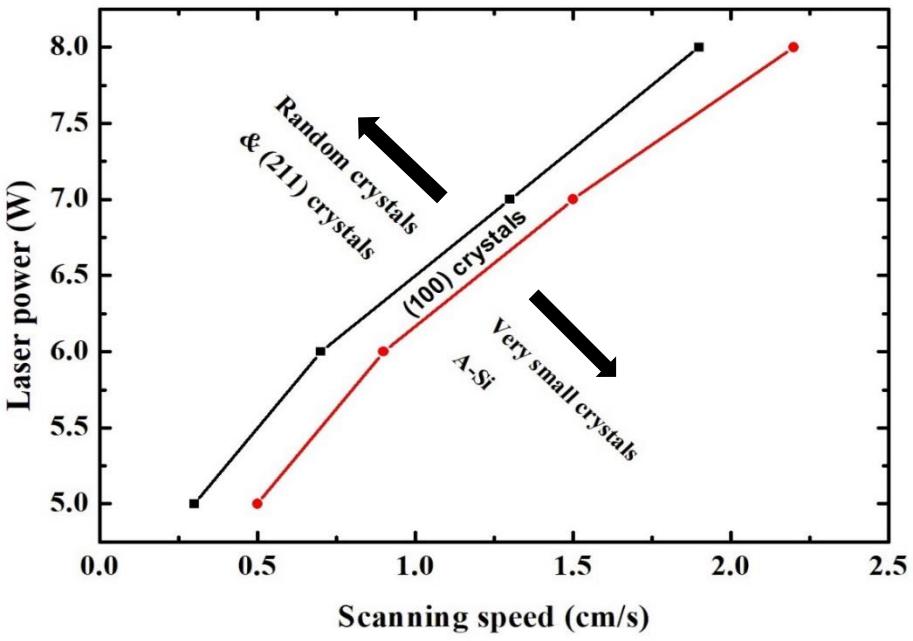

Fig. 3.9 Laser power and scanning speed dependence of crystal orientation

Figure 3.9 shows the dependence of the crystal orientation of the poly-Si thin films on the laser power and scanning speed. The above results show that (100) crystals were realized at 6 W and 0.7 to 0.9 cm/s. And they became minor orientation in the films as

the scanning speed got lower than 0.5 cm/s. With a minor laser power change of under 0.1 W, the (100) preferential orientation was relatively stable. However, with a remarkable power change of over 0.5 cm/s, the preferential orientation was changed. Therefore, as the laser power was considerably varied, the scanning speed was also changed to investigate the crystallinity of the poly-Si thin films. We found that the poly-Si thin films had (100) orientation preference at a narrow band of crystallization conditions of above the threshold for sequential-lateral crystallized Si shown in Fig. 3.9. Under this band, mixed-phase crystallizations consisting of lateral and solid-phase crystallizations occurred or the a-Si still existed in the films. Near the upper edge of this band, randomly orientated crystals were typically observed. And predominantly (211)-(110)-(111) oriented crystals were formed at a high laser power and low scanning speed.

3.4 Conclusions

The effect of crystallization conditions including overlapping scanning, scanning speed, and laser power on the crystallinities of the laser- crystallized poly-Si films were investigated. We found that these conditions were major factors for the preferential orientation of the poly-Si thin films. The crystallinity of the laser-crystallized poly-Si films was strongly dependent on the scanning speed and laser power. The poly-Si thin films had (100) orientation preference at a narrow-limited band of crystallization conditions of above the threshold for sequential-lateral crystallized Si. Under this band, mixed-phase crystallizations consisting of lateral and solid-phase crystallizations occurred or the a-Si still existed in the films. Near the upper edge of this band, randomly orientated crystals were typically observed. And predominantly (211)-(110)-(111) oriented crystals were formed at a high laser power and low scanning speed. The predominantly (100) surface orientation of the poly-Si film was stable with overlapping scanning. By increasing overlapping ratio, the sequential-lateral crystallized Si regions were enlarged and (100) crystals were developed in large areas. However, the (100) crystals were rotated around <001> from (100) to (110) and the in-plane orientation of the film was changed. The mechanism of (100) texture formation and orientation preference of the poly-Si thin film formed by the MLB-CLC and the meaning of

predominantly (100) oriented poly-Si thin films for the performance enhancement of the TFTs would be discussed in the chapter 5.

References

[1] J. N. Lee, B. J. Lee, D. G. Moon, and B. T. Ahn, "*Effect of Deposition Temperature on the Crystallization Mechanism of Amorphous Silicon Films on Glass,*" Jpn. J. Appl. Phys. **36**, 6862(1997).

[2] G. Huang, Z. Xi, and D. Yang, "*Crystallization of amorphous silicon thin films: The effect of rapid thermal processing pretreatment,*" Vacuum **80**, 415(2006).

[3] S. D. Brotherton, D. J. Mcculloch, and J. P. Gowers, "*Influence of Excimer Laser Beam Shape on Poly-Si Crystallisation,*" Jpn. J. Appl. Phys. **43**, 5114(2004)

[4] G. Fortunato, L. Mariucci, R. Carluccio, A. Pecora, and V. Foglietti, "*Excimer laser crystallization techniques for polysilicon TFTs,*" Appl. Surf. Sci. **154-155**, 95 (2000).

[5] N. Matsuo, Y. Aya, T. Kanamori, T. Nouda, H. Hamada, and T. Miyoshi, "*Study of Crystal Growth Mechanism for Poly-Si Film Prepared by Excimer Laser Annealing,*" Jpn. J. Appl. Phys. **39**, 351(2000).

[6] James S. Im, M. Chahal, P.C. van der Wilt, U.J. Chung, G.S. Ganot, A.M. Chitu, N. Kobayashi, K. Ohmori, A.B. Limanov, "*Mixed-phase solidification of thin Si films on* SiO_2", J. Crys. Growth **312**, 2775(2010).

[7] N. Sasaki, Y. Nieda, D. Hishitani, Y. Uraoka, "*Power dependence of orientation on low-temperature poly-Si lateral grains crystallized by a continuous-wave laser scan,*" Thin Solid Films **631**, 112(2017).

[8] T. T. Nguyen, M. Hiraiwa, T. Koganezawa, S. Yasuno, and S.-I. Kuroki, "*Formation of (100)-oriented large polycrystalline silicon thin films with multiline beam continuous-wave lateral crystallization*," Jpn. J. Appl. Phys. **57**(3), 031302-1-031302-6 (2018).

[9] M. C. Morris, H. F. McMurdie, E. H. Evans, B. Paretzkin, J. H. de Groot, B. S. Weeks, and R. J. Newberry, "*Standard X-ray Diffraction Powder Patterns,*" Natl. Bur. Stand. (U.S) Monogr. **25**, 13, 35 (1976).

Chapter 4: Ultrahigh-Performance Poly-Si Thin Film Transistors with Highly (100)-surface Oriented Poly-Si Thin Films.

4.1 Introduction

In chapter 2 and 3, methods and crystallization conditions for forming (100) poly-Si thin films using MLB-CLC and controlling the preferential orientation were discussed. Highly (100)-bi-axially oriented poly-Si thin films were obtained at low laser energy regime of above the threshold for lateral crystallized Si. Highly (211)-(110)-(111) oriented poly-Si thin films were formed at high energy regime. Between low and high energy regimes, the orientation preference was not seen. Mixed crystals of various surface orientations such as (100), (311), (211), and (110) were observed. Highly (100) surface large poly-Si thin films with high biaxial tensile strain were very important for high-performance TFTs. Ultrahigh electron field effect mobility TFTs of approximately 1000 cm^2/Vs fabricated with (100) silicon crystals have been reported [1-5]. This mobility is extremely higher than that of bulk silicon device. However, the disadvantages of technologies, which were applied in those reports, were necessity of SiO_2/Si structure and unpopularity of (100) crystals. Hence, the (100) preferentially poly-Si thin films formed by the MLB-CLC becomes the most potential candidate for practical applications. The above reported results have been proved that high biaxial tensile strain brought about the mobility enhancement. It is believed that high electron mobility LTPS-TFTs could be realized on these films because (100) crystals had a larger size than the feature size of channels. In this research, we fabricated LTPS-TFTs on (100) poly-Si thin films with a simple-low temperature process of under 550 ^oC and ultrahigh-performance LTPS-TFTs were achieved. The characteristics of TFTs would be reported in this chapter. High electron mobility TFTs would precisely be characterized. In addition, the surface orientation dependence of electron mobility would be shown.

4.2 Experimental

4.2.1 Preparation of (100) oriented poly-Si thin films

Poly-Si thin films were prepared as follows: 150 nm a-Si thin films with 100 nm cap SiO_2 deposited on the SiO_2 buffers of quartz substrates were prepared for laser crystallization as shown in the 2.1.1 in chapter 2. After being annealed at 490^oC for an

hour, the a-Si films were crystallized by the MLB-CLC. The laser crystallization conditions were 6 W laser power, 0.8 cm/s scanning speed, and 83% overlapping ratio. At these conditions, lateral-crystallized Si was obtained and (100) textures were dominant in the whole poly-Si film shown in the 2.3.1 in chapter 2. Then, the cap SiO_2 were completely removed by BHF etching to prepare for TFT fabrication.

4.2.2 TFTs fabrication

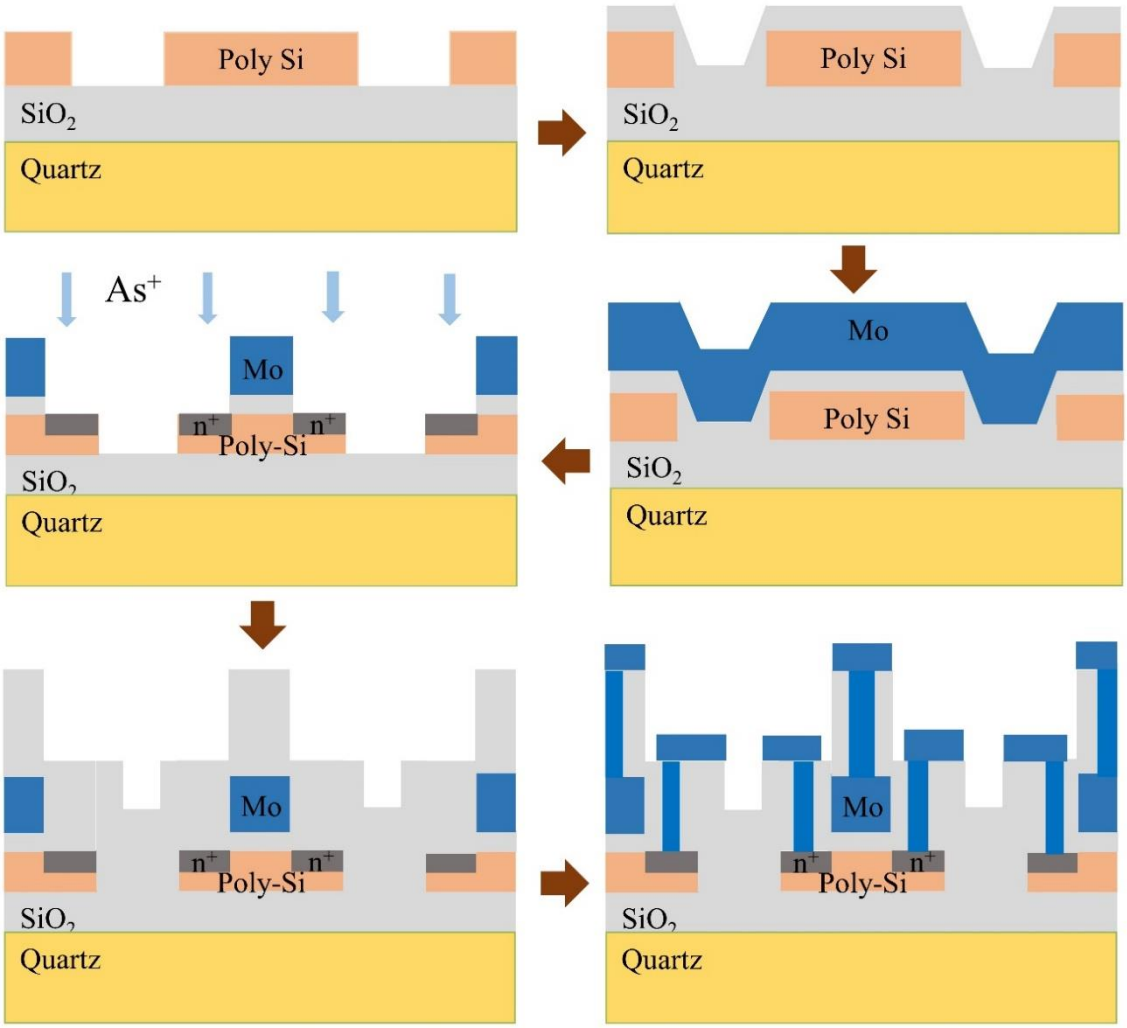

Fig. 4.1. a) Schematic of TFT fabrication process

After the cap SiO_2 layer was etched, the poly-Si active layer was patterned using photolithography and dry etching (Cl_2: 20 sccm, HBr: 20 sccm). Gate oxide SiO_2 of 42 ± 2 nm thickness was deposited by remote Plasma-Enhanced Chemical Vapor Deposition

(remote PECVD) at 300° C (SiH_4: 0.6 sccm, O_2: 10 sccm, Ar: 40 sccm). A Mo gate electrode of 300 nm thickness was deposited by sputtering. Patterning of the gate electrodes was carried out by photolithography and wet etching (H_3PO_4:HNO_3:CH_3COOH:H_2O = 400:25:50:25), followed by a self-aligned source and drain formation by As ion implantation for n-channel TFTs (dose: 2 x 10^{15} cm^{-2}, accelerating voltage: 66 kV) and B ion implantation for p-channel TFTs (dose: 2 x 10^{15} cm^{-2}, accelerating voltage: 13 kV) with the Mo gate as a mask.

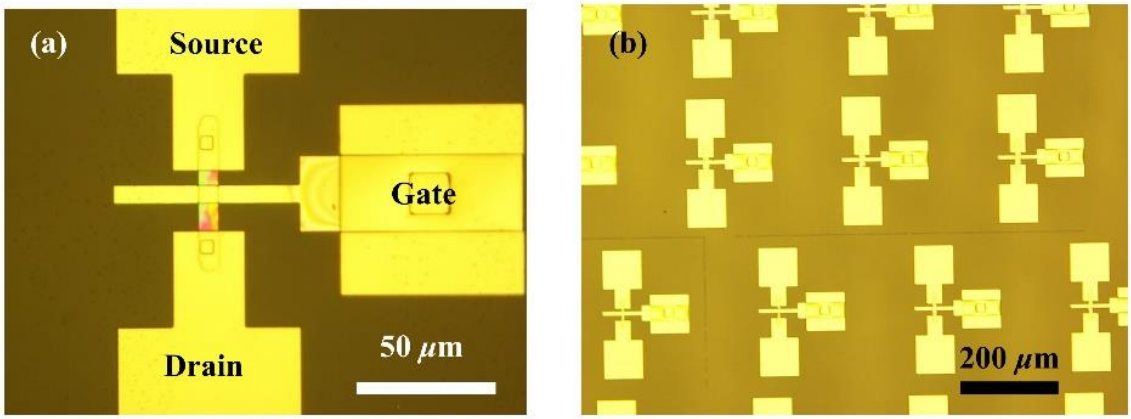

Fig. 4.2. Microphotographs of the fabricated poly-Si TFT [6].

Activation annealing treatment was performed at 550° C in N_2 ambient for 30 minutes. Before SiO_2 interlayer dielectric film of 600 nm thickness was deposited by Atmospheric Pressure Chemical Vapor Deposition (APCVD), sacrificial SiO_2 in the source and drain region was etched by the BHF. The contact hole was formed by lithography and BHF wet etching. A Mo metal pad of 700 nm thickness was deposited by sputtering and patterned by lithography and wet etching. Finally, the sample was annealed at 400° C in H_2 ambient for 30 minutes. In these processes, the grain boundaries were partially pacified by the gate SiO_2 deposition with remote PECVD and the H_2 annealing. The highest temperature in the whole processes was 550° C. The channel were designed with the width of W = 3, 5, 10, 20 μm and the length of L= 10 μm. Both parallel and perpendicular TFTs were fabricated. Figure 4.1 shows the schematic of TFT fabrication process flow. The photomicrographs of the fabricated TFTs are shown in Fig. 4.2. In the poly-Si thin films, Si crystal grains were elongated in the laser scanning direction. In the TFTs, the channel

direction from the drain region to the source region was fabricated as parallel and perpendicular to this direction.

4.3 Results and discussions

4.3.1 Characterization of parallel n-channel TFTs

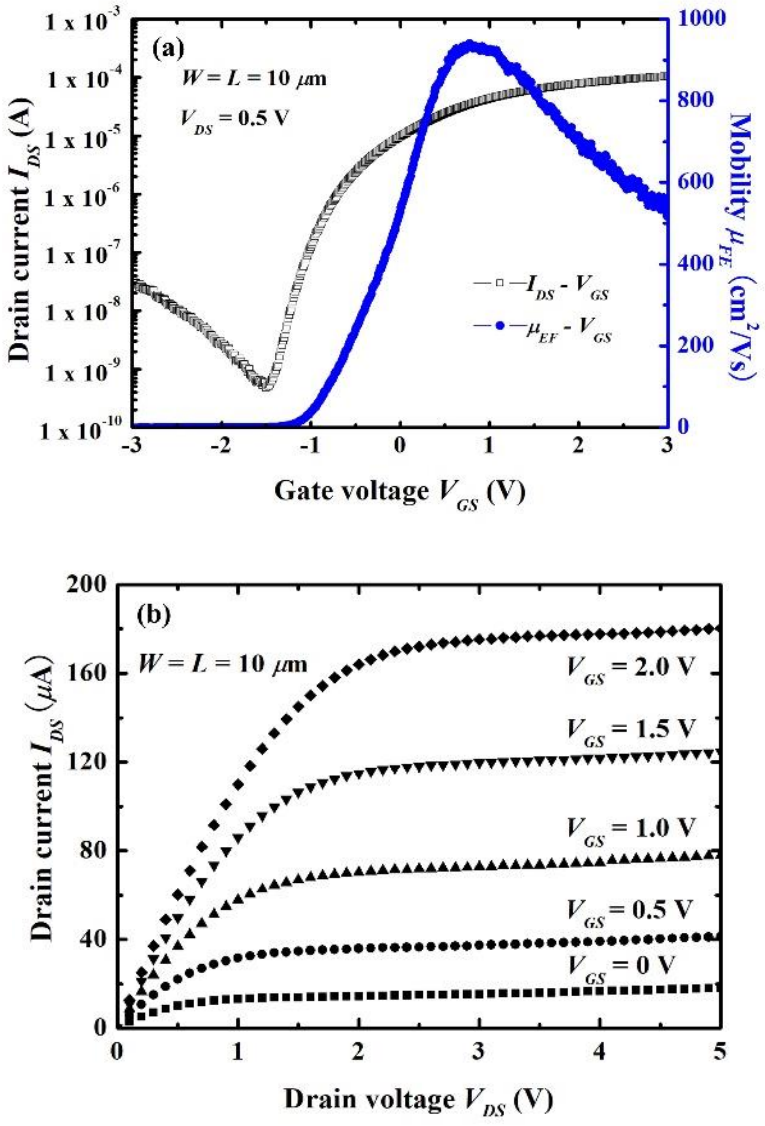

Fig. 4.3. (a) I_{DS}-V_{GS} characteristics, (b) I_{DS}-V_{DS} characteristics of a typical fabricated laser-crystallized poly-Si TFT (L=W=10 μm) [6].

Figures 4.3(a) and 4.3(b) show drain current (I_{DS}) versus gate voltage (V_{GS}) and (I_{DS}) versus gate voltages (V_{DS}) characteristics, respectively, of a typical fabricated parallel TFT with W = 10 μm and L = 10 μm. As predicted, ultra-high performance TFTs were achieved with a predominantly (100) oriented poly-Si thin film. The I_{DS}-V_{GS} relationship at V_{DS} = 0.5 V on an exponential scale indicated an ON/OFF current ratio of 10^5, a threshold voltage (V_{th}) of -0.8 V, and a sub-threshold slope (S) of 0.15 V/dec. The curve of the electron field effect mobility (μ_{FE}) versus V_{GS} shown in Fig. 4.3(a) shows an ultra-

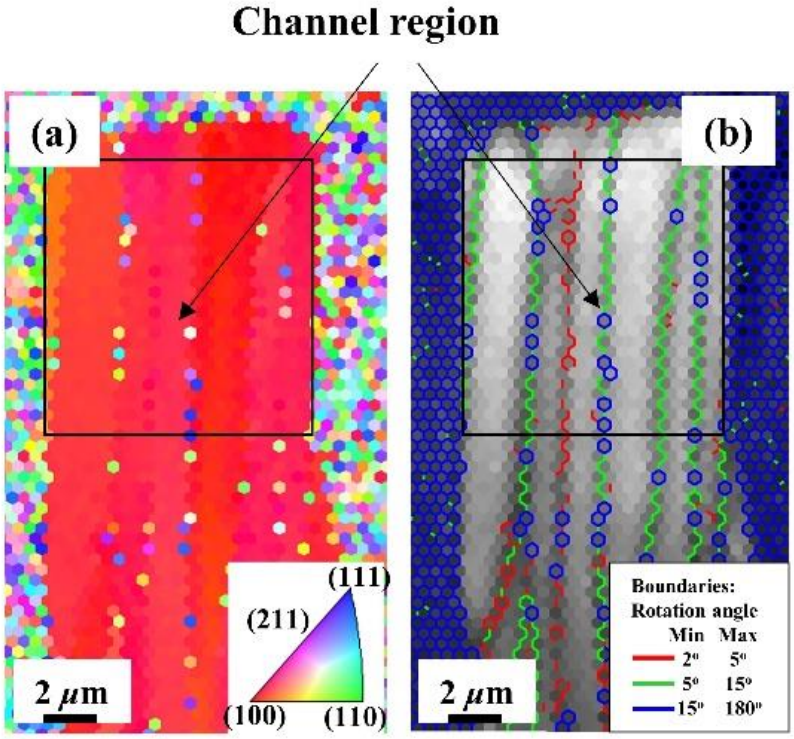

Fig. 4.4. (a) Grain mapping, (b) grain boundary mapping measured by EBSD of a high performance TFT [6].

high mobility of 940 cm^2/Vs, which was achieved with the (100) surface oriented poly-Si film TFTs. In addition, operations of linear and saturation were indicated in the curve of I_{DS} versus V_{DS} at increasing V_{GS} in steps of 0.5 V beginning from 0 V as shown in Fig. 4.3(b). These results are comparable to single crystal devices. In our TFTs, the channel direction was parallel to the laser scanning direction, and then the linear grain boundaries were laid on the channel parallel to the direction of the current flow. The parallel linear grain boundaries did not induce the grain boundary scattering at the carrier drifting that

have been observed in conventional poly-Si TFTs [7]. As a result, the characteristics show high electron mobility which is comparable to Si single crystals.

The electron field effect mobility depends on crystal orientation, grain boundaries, and tensile strain of the poly-Si film in the channel region [7-10]. To study the enhancement mechanism of the TFTs' electron mobility, we investigated crystallinity and tensile strain of the poly-Si film in the channel regions. The crystallinity was measured by EBSD. The EBSD measurement was carried out after removal of the TFTs' gate electrode and oxide. Figures 4.4(a) and 4.4(b) show grain mapping in the normal surface direction and grain boundary mapping of a typical TFT observed by EBSD. It was found that at the TFTs with high mobility of over 900 cm^2/Vs, the (100) surface orientation has a dominant area in the whole channel as shown in Fig. 4.4(a). The channel region included seven Si (100) crystal grains with an approximately 20 μm length that is longer than the channel length of 10 μm. It can be assumed that the TFT consists of 7 single crystal TFTs, and the mobility is approximately observed as the Si (100) single crystal mobility. It is well known that (100) surface orientation gives the lowest electron effective mass and a lower surface energy at the interface. A maximal value of the mobility is hence obtained with Si (100) crystallites [8-14]. Moreover, because of no coincident site lattice (CSL) grain boundaries, the boundary mapping was shown with rotation angles between neighboring crystal grains (Fig. 4.4(b)). The red, green, and blue boundaries had disorientation angles of $2^o - 5^o$, $5^o - 15^o$, and above 15^o, respectively. A red boundary and five green were observed in the channel region. These grain boundaries are the low-angle Read-Shockley mixed type and parallel to the direction of the current flow. They have low electrical activity and can be constructed without any dangling bonds [15,16]. The TFT's effective channel width can be presumed as its geometric channel width. This result indicates that carrier transport is not affected by grain boundary barriers. On the other hand, in the red boundary, one unit cell of crystal grain was tilted against other unit cells of the neighboring grain. In the five green boundaries, over 20 unit cells were tilted against other unit cells of neighboring grains.

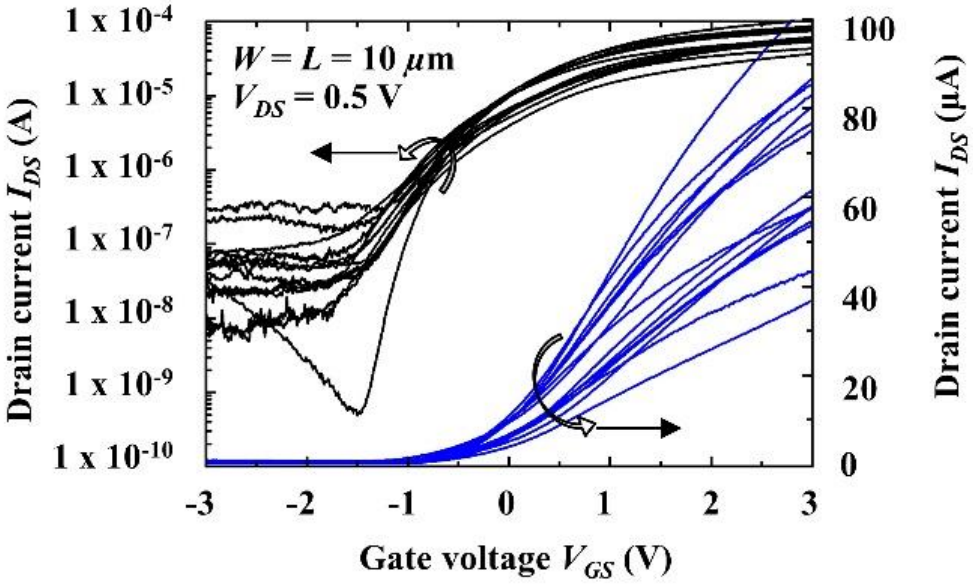

Fig. 4.5 I_D-V_G characteristics of the laser-crystallized poly-Si TFTs.

Table 4.1 Average performance of the poly-Si TFTs and their variation

Maximum Mobility μ_{FE} ($cm^{-2}V^{-1}s^{-1}$)	1010
Average mobility μ_{FE} ($cm^{-2}V^{-1}s^{-1}$)	616 ± 164
Subthreshold slope (*S*) (mV/dec)	473 ± 183
ON/OFF ratio	$10^2 \div 10^5$
Threshold voltage *Vth* (V)	-1.2 ± 0.2

Figure 4.5 shows drain current (I_{DS}) versus gate voltages (V_{GS}) and characteristics of a fabricated TFT group with W = 10 μm and L = 10 μm on linear and exponential scales. High performance was achieved in most of TFTs, however, their variation was high. The high variation results from the difference of the crystal orientation in the channels, the type and number of grain boundaries, and the density of voids in the channel regions. Therefore, the poly-Si TFTs had various electron field effect mobility values. The results of the evaluation of average performances and their variation of 67 TFTs are summarized in Table I. In this work, the electrical properties of TFTs show an excellent electron field

effect mobility with its average value of 616 cm^2/Vs and standard deviation (± σ) of 164 cm^2/Vs. However, a high average subthreshold slope (*S*) of 473 mV/dec and its high variation (± σ) of 183 mV/dec was found. In addition, rather high leakage currents and low ON/OFF ratios were observed in the TFTs.

Figure 4.6(a) shows the mobility distribution of $\Delta\mu$ = 100 cm^2/Vs for 67 devices. This graph indicates the electron field effect mobility distributed in two ranges among 300

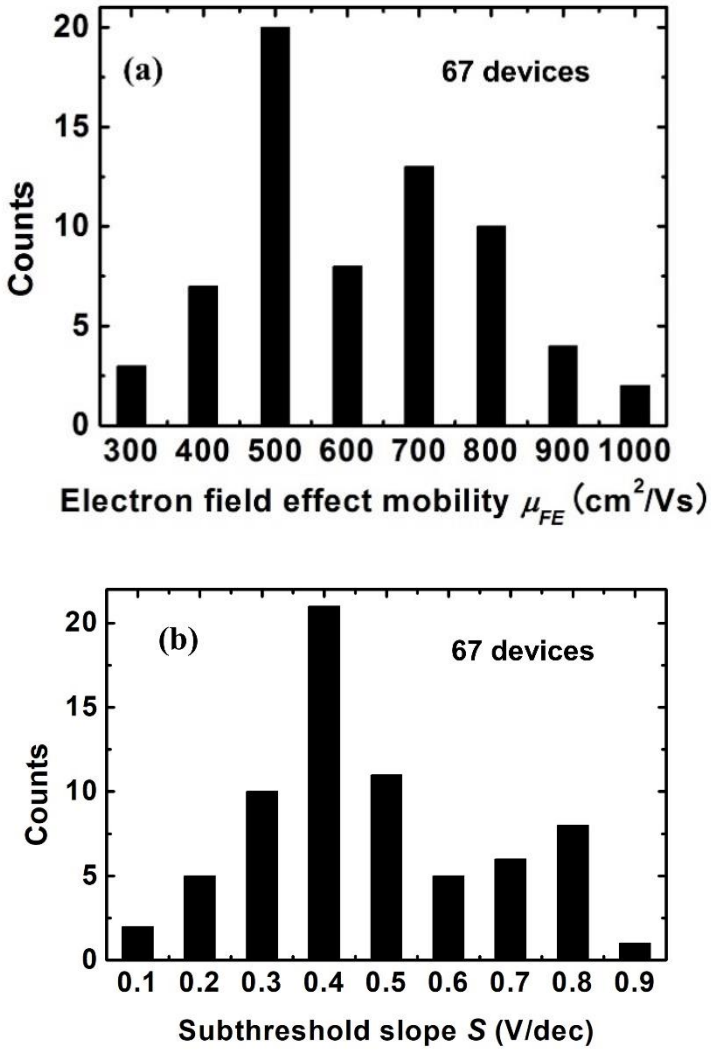

Fig. 4.6 (a) Distribution of TFT devices as a function of mobility, (b) distribution of TFT devices as a function of sub-threshold slope [6].

cm^2/Vs and 1000 cm^2/Vs. The former range of under 600 cm^2/Vs reached a peak of 500 cm^2/Vs. The later of over 600 cm^2/Vs, which represented 50% of all devices, reached

maximum number at 700 cm^2/Vs. For reproducibility of the CLC technology, we can improve uniformity of the poly-Si TFTs by controlling the position of the voids to out of channel regions and crystallinity of the poly-Si film. This technology is promising for the operation of larger applications of the poly-Si TFTs in the future. Figure 4.6(b) shows the sub-threshold slope distribution of ΔS = 0.1 V/dec for 67 devices with a fitted Gaussian distributed graph. It appears that the sub-threshold slope distributed in a wide range from 0.1 V/dec to 0.9 V/dec. The subthreshold slope reached maximum number at 0.4 V/dec.

Figure 4.7 shows the relation between the mobility and S factor. In the range of ultra-high mobility of over 800 cm^2/Vs, TFTs had low S factors. At low mobility TFTs, apparent correlation between the S factor and the mobility was however not found. The high TFTs' performance variation can be illuminated by the crystallinities of the poly-Si films. When the channel consists of differently oriented crystallites, high-angle grain boundaries are found. Both low-angle and high-angle grain boundaries may exist in the poly-Si film. They can be longitudinal or latitudinal grain boundaries. Some of these may

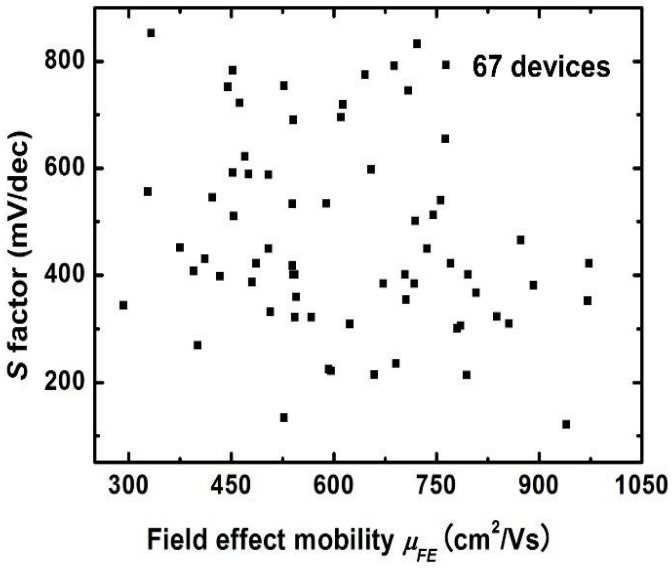

Fig. 4.7 Plot of S factors versus electron field effect mobility [6]

cross the current flow. The high-angle grain boundaries cause trap states originated from the Si dangling bonds and distorted bonds which have an energy state near the middle of the Si band gap [17,18]. As these grain boundaries cross the current flow, they make a high barrier potential and significantly reduce the mobility. Accordingly, the mobility is

not only reduced but also the sub-threshold slope and the leakage current are increased. To improve the sub-threshold slope and the leakage current, an activation treatment on the trap states should be performed. A high-pressure H_2O vapor annealing and Boron implantation can be applied [19,20]. In addition, the crystal defects including voids and crystal dislocations at the grain boundaries partially bring about the variation of devices. For reproducibility of the CLC technology, we can improve uniformity of the poly-Si TFTs by controlling the position of the voids to out of channel regions and crystallinity of the poly-Si film. This technology is promising for the operation of larger applications of the poly-Si TFTs in the future.

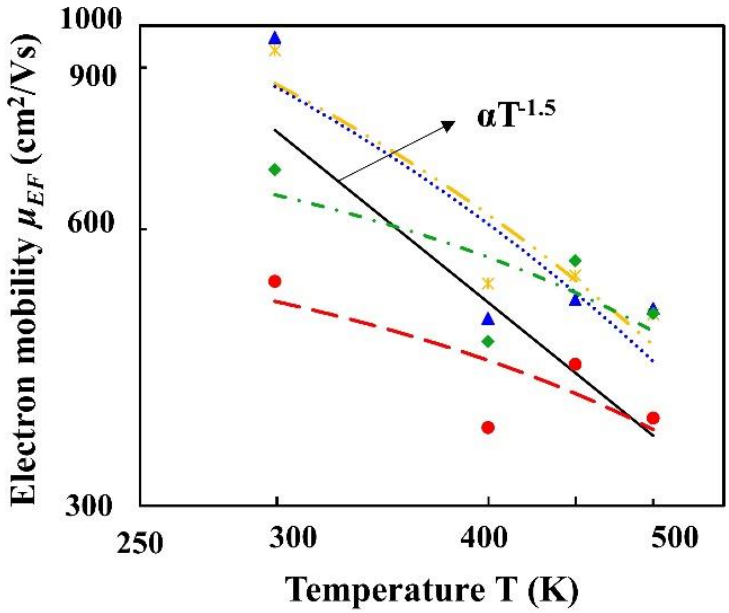

Fig. 4.8 Temperature dependence of electron field effect mobility.

Figure 4.8 shows the dependence of electron field effect mobility on temperature in some typical TFTs. The temperature was varied from room temperature to 200°C. It appears that the mobility decreased with the increase of the temperature as the exponential function of the temperature. The exponential coefficients were approximate -1.5. The higher mobility the TFTs have, the smaller their exponential coefficient is. This result indicates that phonon scattering was dominant in the TFTs. The phonon scattering in ultrahigh-mobility TFTs was more dominant than that in others.

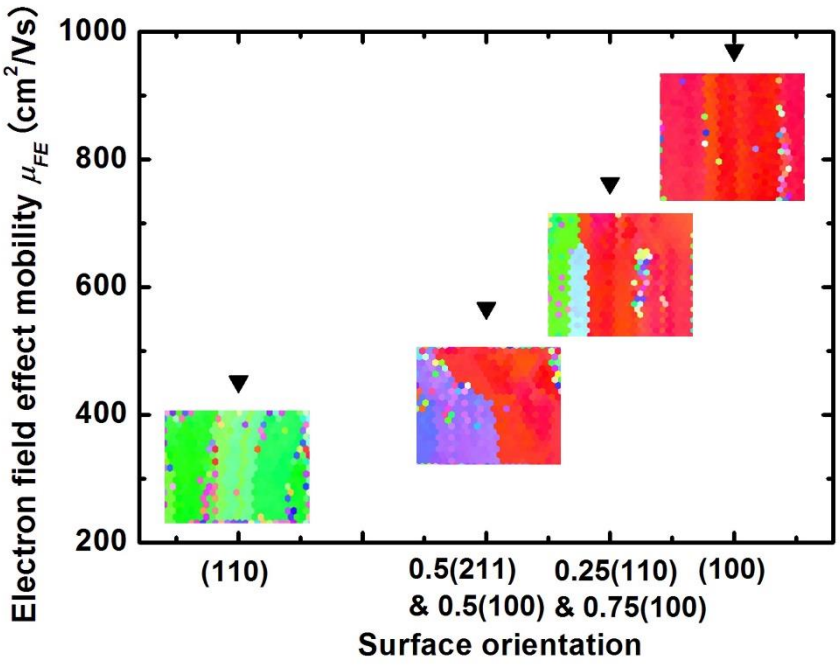

Fig. 4.9 Correlation between crystal orientation and electron field effect mobility [6].

The correlation between the microscopic crystallinity of TFTs and the TFTs' performance is shown in Fig. 4.9. In particular, mobility reached a peak of 971 cm^2/Vs due to Si crystal oriented (100) plane in the whole channel. As (100) orientation (red region) decreased, TFT mobility reduced. With orientation of all Si crystals at almost (110) plane, the device had a minimum mobility of 452 cm^2/Vs. This graph shows that (100) surface orientation is the decisive factor of ultra-high performance poly-Si TFTs. The ratio of the mobility of the (100) and (110) surface oriented poly-Si TFTs (μ(100)/μ(110)) was approximately 2.2. These results are in good agreement with previous findings of Si single crystal devices.[10] On the other hand, as (100) orientation (red region) partially occupied the channel and others appeared, the μ(100)/μ(110) ratio was not in the law of Si single crystal devices because of an appearance of both high-angle and low-angle grain boundaries across a part of the current flow and voids in the channel. Consequently, the mobility was significantly reduced.

4.3.2 Characterization of perpendicular n-channel TFTs

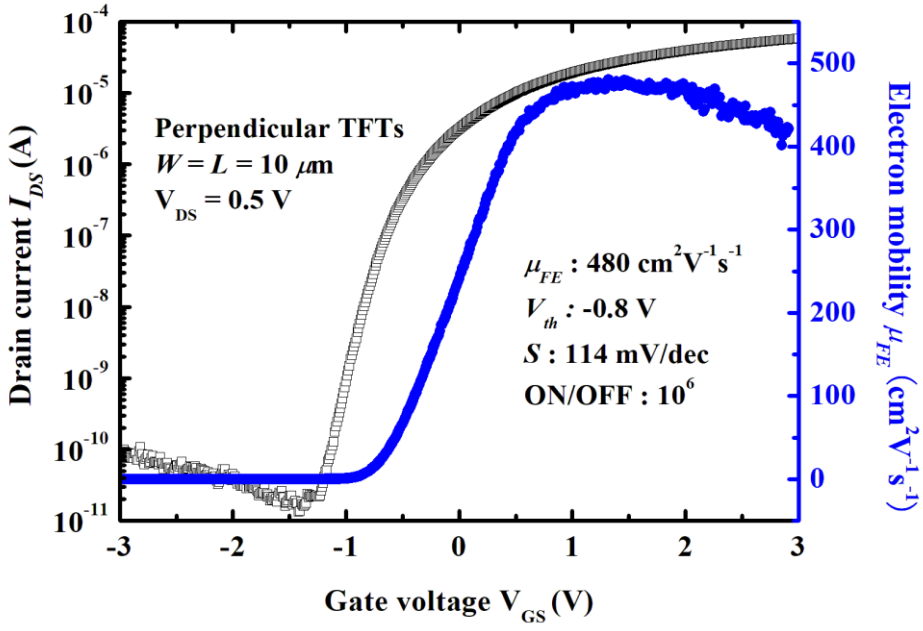

Fig. 4. 10 I_{DS}-V_{GS} characteristics of a typical perpendicular TFT.

Figures 4.10 shows drain current (I_{DS}) versus gate voltages (V_{GS}) characteristics of a typical fabricated perpendicular TFT with W = 10 μm and L = 10 μm. The TFT had ON/OFF current ratio of 10^6, a threshold voltage (V_{th}) of -0.8 V, and a sub-threshold slope (S) of 114 mV/dec. The curve of the electron field effect mobility (μ_{FE}) versus V_{GS} shows a mobility of 480 cm^2/Vs. This mobility is twice smaller than that of parallel TFTs shown in the 4.3.1. This result illustrates a strong effect of grain boundaries on the electron mobility. Crystal grains averagely had 2 µm width and 20 µm length. Contrary to parallel TFTs, perpendicular TFTs had grain boundaries crossed the current flow of 10 μm length channels. These crossed grain boundaries induced barrier potentials and reduced the mobility. The misorientation angles of the grain boundaries between (100) crystals were small. They induced few grain boudary trap states, few donor concentrations, and insignificant grain boudaries scattering. Therefore the TFT had a small subthreshold slope and a low leakage current.

Table 4.2 average performances and their variations of perpendicular TFTs

Maximum Mobility μ_{FE} ($cm^{-2}V^{-1}s^{-1}$)	518
Average mobility μ_{FE} ($cm^{-2}V^{-1}s^{-1}$)	329 ± 112
Subthreshold slope (*S*) (mV/dec)	517 ± 344
ON/OFF ratio	$10^2 \div 10^8$
Threshold voltage *Vth* (V)	-1.3 ± 0.3

As a result of a strong grain boundary effect, the perpendicular TFTs had a low average performance and high variation, as shown in table 4.2. The average electron mobility of perpendicular TFTs of (100) poly-Si thin films was twice lower than that of parallel TFTs. Their average subthreshold slope and its variation was also higher. In the (100)-surface oriented poly-Si thin films, some regions had (100)-(100)-(100) crystals with low angle grain boundaries. Others had (100)-surface oriented crystals with various orientations in the scanning and transverse directions induced high angle grain boundaries. High angle cross grain boundaries induced high barrier potential, considerably reduced their conductivity, and deduced electron mobility. On the other hand, some perpendicular TFTs had a high mobility. Their mobility was even higher than the maximum electron mobility of parallel TFTs fabricated on (211)-(110)-(111) oriented poly-Si films.

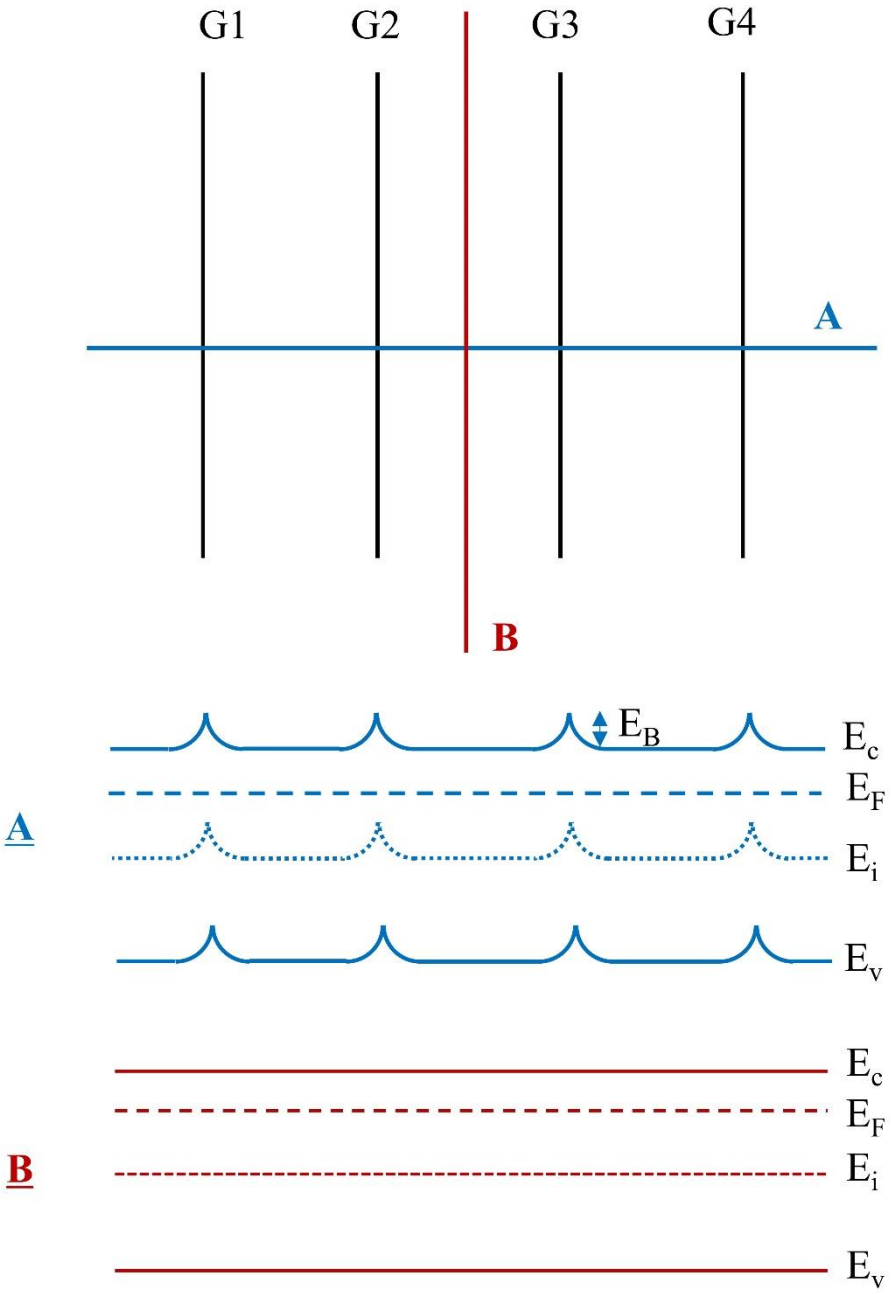

Fig. 4.11 Band diagram of grain boundaries in perpendicular and parallel TFTs.

Figure 4.11 shows band diagram of grain boundaries in perpendicular and parallel TFTs. The A and B show the current flow in perpendicular and parallel TFTs, respectively. The E_B is grain boundary barrier. The conductivity is deduced as the exponential function of the grain boundary barrier (E_B) [6].

4.3.3 Characterization of p-channel TFTs

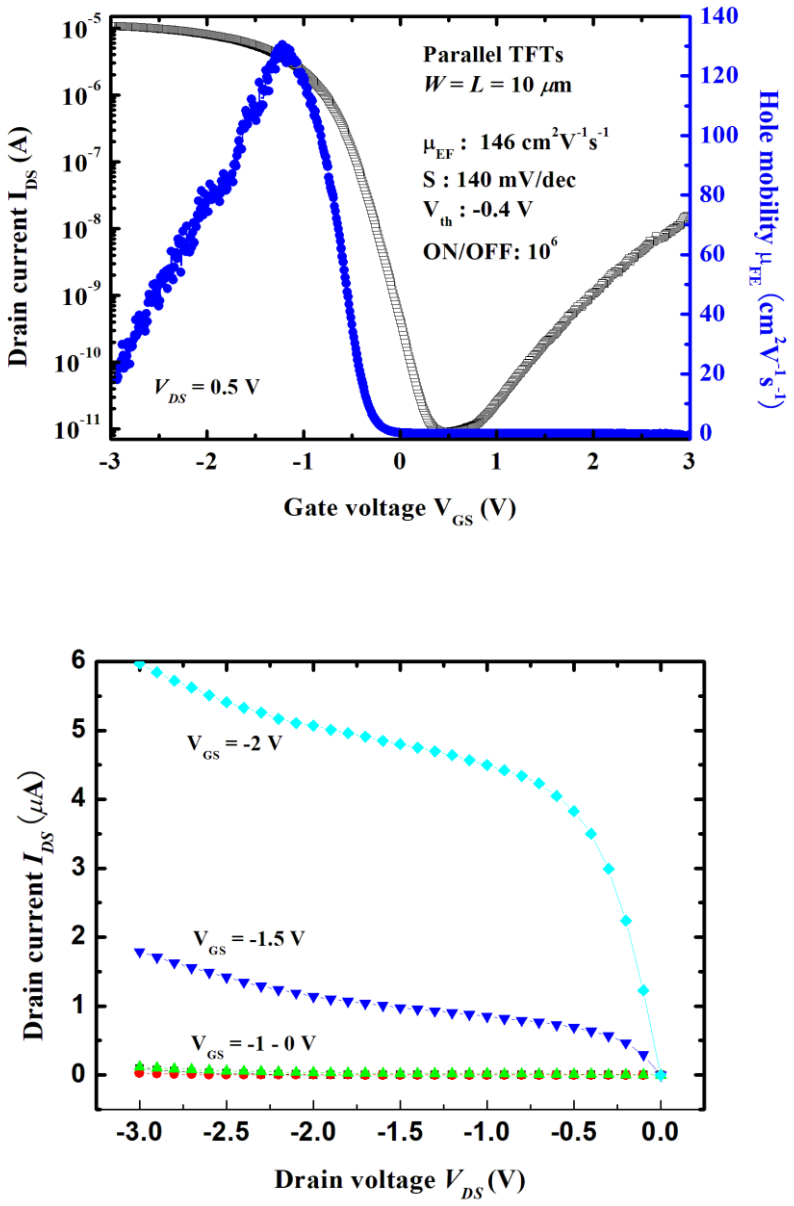

Fig. 4. 12 I_{DS}-V_{GS} and I_{DS}-V_{DS} characteristics of a typical parallel p-channel TFT.

Figures 4.12(a) and 4.12(b) show drain current (I_{DS}) versus gate voltages (V_{GS}) and (I_{DS}) versus gate voltages (V_{DS}), characteristics of a typical fabricated parallel p-channel TFT with a same channel size with n-channel TFTs (W = 10 μm and L = 10 μm). The I_{DS}-V_{GS} relationship at V_{DS} = 0.5 V on an exponential scale indicated an ON/OFF current ratio

of 10^6, a threshold voltage (V_{th}) of -0.4 V, and a sub-threshold slope (S) of 0.14 V/dec. The curve of the hole field effect mobility (μ_{FE}) versus V_{GS} shows the hole mobility of 146 cm^2/Vs. This mobility is extremely lower than the electron mobility. In addition, operations of linear and saturation were indicated in the curve of I_{DS} versus V_{DS} at increasing V_{GS} in steps of 0.5 V beginning from 0 V as shown in Fig. 4.12(b). The I_{DS} was negligible as the V_{GS} of over -1 V.

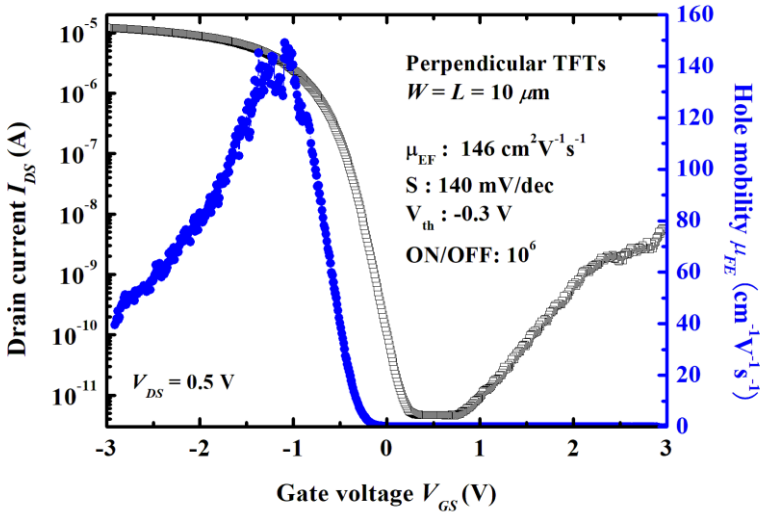

Fig. 4.13 I_{DS}-V_{GS} characteristics of a typical perpendicular p-channel TFT.

Fig 4.13 shows I_{DS}-V_{GS} characteristics of a typical perpendicular p-channel TFT with the same channel size with parallel TFTs (W = 10 μm and L = 10 μm). It appears that characteristics of parallel and perpendicular TFTs were similar. They had an almost same hole mobility, subthreshold slope, ON/OFF ratio, and threshold voltage.

Table 4.3 Average performance and its variation of parallel p-channel TFTs (W = 3 μm, L = 10 μm)

Maximum Mobility μ_{FE} ($cm^{-2}V^{-1}s^{-1}$)	230
Average mobility μ_{FE} ($cm^{-2}V^{-1}s^{-1}$)	148 ± 46
Subthreshold slope (S) (mV/dec)	117 ± 21
ON/OFF ratio	10^5-10^6
Threshold voltage Vth (V)	0.3 ± 0.2

The p-channel TFTs with W = 3 μm had better characteristics than others. Their average performances and their variation are summarized in Tab. 4.3. It is found that their average hole mobility was low and its deviation was large. However, they had good threshold slope and high ON/OFF ratio. The highest hole mobility of 230 $cm^{-2}V^{-1}s^{-1}$ was realized. This mobility was similar to that in the previous report of A. Hara et al. [20].

4.4 Conclusions

With the low temperature fabrication process, parallel and perpendicular n-channel TFTs were fabricated on highly (100) surface oriented poly-Si thin films. Ultrahigh-performance TFTs were achieved with ultrahigh electron field effect mobility of up to 1010 cm^2/Vs. An excellent subthreshold slope of 0.15 V/dec, a high ON/OFF ratio of 10^5, and a threshold voltage of -0.8 V were also obtained. The crystallinities of the poly-Si channels of the TFTs were characterized. It indicates that (100) crystals with parallel low-angle grain boundaries and high biaxial tensile strain brought about ultrahigh electron mobility. In addition, the correlation between the surface orientation of the poly-Si film and electron mobility was described. The ratio of μ(100)/μ(110) was found in good agreement with c-Si devices. However, numerous TFTs had low mobility and induced a high variation in the TFTs' performance because their poly-Si channels had other orientations and consisted of high angle grain boundaries. On the other hand, void appearance in the poly-Si channels also deduced the variation. High performance perpendicular TFTs were also achieved on these films. They had maximal electron field

effect mobility of 518 cm^2/Vs. This mobility was twice smaller than that of parallel TFTs. They also had excellent subthreshold slope and high ON/OFF ratio. However, their performance variation was higher than that of parallel TFTs due to strong effect of cross grain boundaries and the difference of misorientation angles at grain boundaries. In addition, p-channel TFTs were also fabricated on (100) poly-Si thin film. The characteristics of p-channel TFTs seem to be contrary with n-channel TFTs. They had very low hole field effect mobility that was much smaller than electron mobility. However, they had low subthreshold slope and high ON/OFF ratio. In addition, the mobilities of parallel and perpendicular TFTs were insignificantly different.

References

[1] T. Chen, R. Ishihara, K. Beenakker, "*Location- and Orientation-Controlled (100) and (110) Single-Grain Si TFTs without Seed Substrate,*" IEEE Trans. Electron Devices **57**, 2348 (2010).

[2] T. Chen, R. Ishihara, J. Cingel, B. Alessandro, M. R. T. Mofrad, H. Schellevis, and K. Beenakker, "*Integrated high performance (100) and (110) oriented single-grain Si TFTs without seed substrate,*" Tech. Dig. Int. Electron Devices Meet., p. 179 (2009).

[3] M. Mitani, T. Endo, S. Tsuboi, T. Okada, G. Kawachi, and M. Matsumura, "*Relationship between Thin-Film Transistor Characteristics and Crystallographic Orientation in Excimer-Laser-Processed Pseudo-Single-Crystal-Silicon Films,*" Jpn. J. Appl. Phys. **49**, 124001 (2010).

[4] M. Mitani, T. Endo, Y. Taniguchi, T. Katou, S. Shimoto, T. Ohno, S. Tsuboi, T. Okada, K. Azuma, G. Kawachi, and M. Matsumura, "*Ultrahigh-Performance Polycrystalline Silicon Thin-Film Transistors on Excimer-Laser-Processed Pseudo-Single-Crystal Films,*" Jpn. J. Appl. Phys. **47**, 8707 (2008).

[5] C-H Chou, W-S Chan, I-C Lee, C-L. Wang, C-Y Wu, P-Y. Yang, C-Y. Liao, K-Y. Wang, and H-C Cheng, "*High-performance Single-Crystal-Like Strained-Silicon Nanowire Thin-Film Transistors via Continuous-Wave Laser Crystallization,*" IEEE Electron Device Lett., **36**, 348 (2015).

[6] T. T. Nguyen, M. Hiraiwa, and S.-I. Kuroki, "*Ultrahigh-performance (100)-oriented polycrystalline silicon thin-film transistors and their microscopic crystal structures*," Appl. Phys. Exp., **10**, 056501 (2017).

[7] J. Levinson, F. R. Shepherd, P. J. Scanlon, W. D. Westwood, G. Este, and M. Rider, "*Conductivity behavior in polycrystalline semiconductor thin film transistors,*" J. Appl. Phys. **53**, 1193 (1982).

[8] T. Satô, Y. Takeishi, and H. Hara, "*Mobility Anisotropy of Electrons in Inversion Layers on Oxidized Silicon Surfaces,*" Phys. Rev. B, **4**(6), 1950(1971).

[9] M. T. Currie, C. W. Leitz, T. A. Langdo, G. Taraschi, E. A. Fitzgerald, and D. A. Antoniadis, "*Carrier mobilities and process stability of strained Si n- and p-MOSFETs in SiGe virtual substrates,*" J. Vac. Sci. Technol. B **19**, 2268 (2001).

[10] S. E. Thompson, S. Suthram, Y. Sun, G. Sun, S. Parthasarathy, M. Chu, and T. Nishida, "*Future of Strained Si/Semiconductors in Nanoscale MOSFETs,*" IEDM Tech. Dig., pp. 1 (2006).

[11] S. Kawamura, J. Sakurai, M. Nakano, and M. Takagi, "*Recrystallization of Si on amorphous substrates by doughnut-shaped cw Ar laser beam,*" Appl. Phys. Lett. **40**, 394 (1982).

[12] C. Spinella, S. Lombardo, and F. Priolo, "*Crystal grain nucleation in amorphous silicon,*" J. Appl. Phys. **84**(10), 5383 (1998).

[13] I. Ohdomari, H. Akatsu, Y. Yamakoshi, and K. Kishimoto, "*The structural models of the Si/SiO_2 interface,*" J. Non-Crys. Solids **89**, 239 (1987).

[14] F. J. Himpsel, F. R. McFeely, A. Taleb-Ibrahimi, and J. A. Yarmoff, "*Microscopic structure of the SiO2/Si interface,*" Phys. Rev. B **38**, 6084 (1988-II).

[15] W. T. Read and W. Shockley, "*Dislocation Models of Crystal Grain Boundaries,*" Phys. Rev. **78**, 275 (1950).

[16] M. Kimura, R. Nozawa, S. Inoue, T. Shimoda, B. O.-K. Lui, S. W.-B. Tam, and P. Migliorato, "*Extraction of Trap States at the Oxide-Silicon Interface and Grain Boundary for Polycrystalline Silicon Thin-Film Transistors,*" Jpn. J. Appl. Phys. 40, 5227(2001).

[17] I. W. Wu, T. Y. Huang, W.B. Jackson, A.G. Levis, and A. Chiang, "*Passivation kinetics of two types of defects in polysilicon TFT by plasma hydrogenation,*" IEEE Electron Device Lett. **12**, 181 (1991).

[18] K. Asada, K. Sakamoto, T. Watanabe, T. Sameshima, and S. Higashi, "*Heat Treatment with High-Pressure H_2O Vapor of Pulsed Laser Crystallized Silicon Films,*" Jpn. J. Appl. Phys. **39**, 3883 (2000).

[19] T. Sameshima, K. Sakamoto, Y. Tsunoda, and T. Saito, "*Improvement in Characteristics of Polycrystalline Silicon Thin-Film Transistors by Heating with High-Pressure H_2O Vapor,*" Jpn. J. Appl. Phys. **37**, L1452 (1998).

[20] A. Hara, M. Takei, F. Takeuchi, K. Suga, K. Yoshino, M. Chida, T. Kakehi, Y. Ebiko, Y. Sano, and N. Sasaki, "*High-Performance Polycrystalline Silicon Thin Film Transistors on Non-Alkali Glass Produced Using ContinuousWave Laser Lateral Crystallization,*" Jpn. J. Appl. Phys. **43**, 1269 (2004).

Chapter 5: Mechanism of (100) Texture Formation and TFTs' Performance Enhancement

5.1 Introduction

In the previous chapters, we illustrate that the (100) oriented poly-Si thin films were formed by the MLB-CLC. We investigated the effect of crystallization conditions on the crystallinities of the poly-Si films. And we successfully fabricated ultrahigh-performance LTPS-TFTs with ultrahigh electron field effect mobility of 1010 cm^2/Vs. These results are very important for the progression of the TFT technology as well as its applications. In order to develop this technology in the future, understanding the mechanism of preferentially (100) texture formation plays an essential role. In addition, the mechanism for the mobility enhancement is also necessary to be clarified. In the above chapters, we partially discussed about the mechanisms. In this chapter, by overviewing the results in the chapters 2-4, we clarified the mechanisms of (100) texture formation, crystallinity enhancement by overlapping process, and mobility enhancement of the (100) poly-Si thin films.

5.2 Mechanism of (100) texture formation

The (100) surface orientation preference was observed at the crystallization conditions of above the threshold for sequential-lateral crystallized Si. The (100) preferential orientation was also achieved in the scanning and transverse directions. This orientation preference was stable in the normal direction, however changed in the scanning and transverse directions with overlapping scanning process. These results suggest that solid-Si surface energy and SiO_2/Si interfacial energy control the (100) surface orientation at the conditions of low laser exposure energy regime. The surface energy depends on the nature of the bonding of the materials. It is anisotropic because it is basically correlated to the number of dangling bonds on the ideal surface. It has been theoretically calculated and measured for surface energy of semiconductors [1-3]. The measured surface energy of the typical orientations of the silicon are summarized in the table 5.1. It shows that the surface energy reached a maximal value at (100) plane. On the other hand, it is demonstrated that the (100)Si/SiO_2 interface has the lowest interfacial energy. The interfacial energy based on the defects formed by unpaired valence electrons that induce defect's trap energy, at the Si/SiO_2 interface [4-7]. With a mixed-phase crystallization

method, Y. Wang at. al. demonstrated the orientation dependence of Si/SiO_2 interfacial energy as in order $\sigma_{(100)} < \sigma_{(211)} < \sigma_{(110)}, \sigma_{(111)}$ [8]. Figure 5.1 shows the schematic of (100) crystal nucleation occurs after a-Si film melt with laser irradiation. Nucleation starts from the Si/SiO2 interface, the Si/SiO_2 lowest interfacial energy controls Si nuclei oriented at (100) as the silicon is crystallized at low laser exposure energy regime. In addition, it has been reported that <100> is the highest growth direction with growth rate ratio of <100>/<110> and <100>/<110> being 2.6 and 19.7, respectively [7,9,10], this is the second factor for (100) crystals predominantly grown in the normal surface direction.

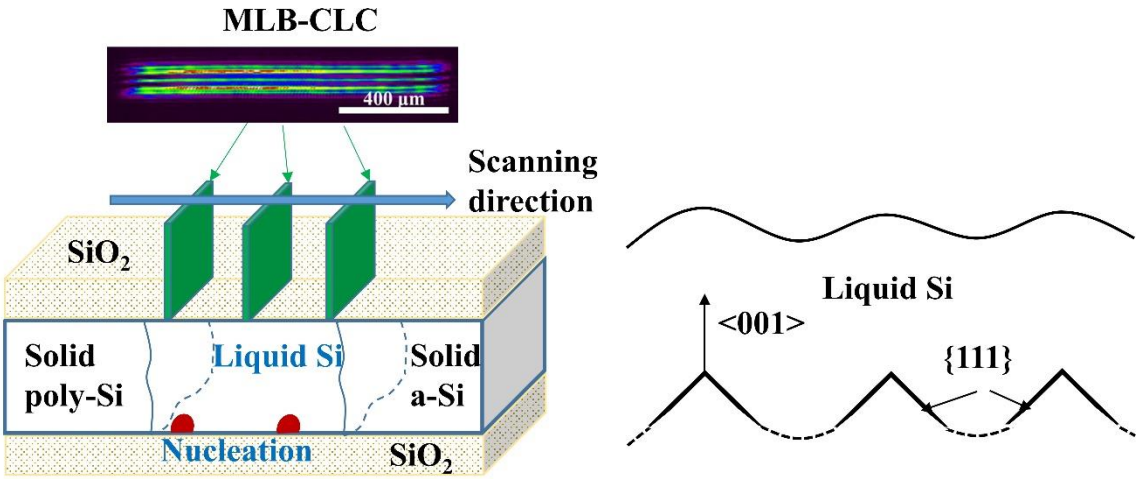

Fig. 5.1 Schematic of (100) crystal nucleation growth after irradiated by laser.

Table 5.1 Surface energy of Si and Ge with typical faces [1]

	(111)	(110)	(100)
Si	1230×10^{-7} (J)	1510×10^{-7} (J)	2103×10^{-7} (J)
Ge	1060×10^{-7} (J)	1300×10^{-7} (J)	1835×10^{-7} (J)

The orientations in the scanning and transverse directions were also (100), however, it seemed to be less stable than the surface orientation and were unstable with overlapping scanning because these preferential orientations were only brought about the highest growth rate of (100) crystals [9,10]. On the other hand, at high laser energy regime, the

orientation of the poly-Si thin films is stable at (211), (110), and (111) in the normal, scanning, and transverse directions. At present, there is no quantitative evidence for the relation between (100) crystal growth and interfacial energy, however, we think that the orders of the interfacial energy and crystal growth rate among the orientations are appropriate to explain for this phenomenon.

5.3 Mechanism of stability of (100) orientation preference with MLB-CLC and overlapping

(211)-(110)-(111)-highly oriented poly-Si thin films were stably formed at a high laser exposure energy regime by single scans [11]. Bi-axially (100) orientation preference was constantly realized at the restricted low laser energy regime. These preferential orientations were really stable. Predominantly (100) crystal formation is explained by solid-Si surface and solid Si/SiO_2 interfacial energies at the above section. However, if it is only based on the Si/SiO_2 interfacial energy, the crystal orientation is sensitive with high laser power. Using MLB-CLC, crystal nucleation can occur at the exposed regions between line-beams. These regions have approximately uniform supercooling temperature, therefore, preferentially oriented crystal nuclei can be grown and control the orientation of the film. The temperature profiles at the exposed region are shown in Fig. 5.2. After being exposed by each single line beam, the temperature of the Si film is promptly dropped and crystal nucleation occurs frequently. In the multi-line beam, the nucleation occurs between line-beam exposures. With low laser exposure energy conditions, the nuclei formed between line-beam exposures can exist during being exposed by the later line-beam because the melting point of crystalline Si is higher than that of a-Si and absorption coefficient of crystalline Si is lower. These crystallization conditions are just above the threshold for melting a-Si; therefore, the (100) crystal nuclei are predominantly developed.

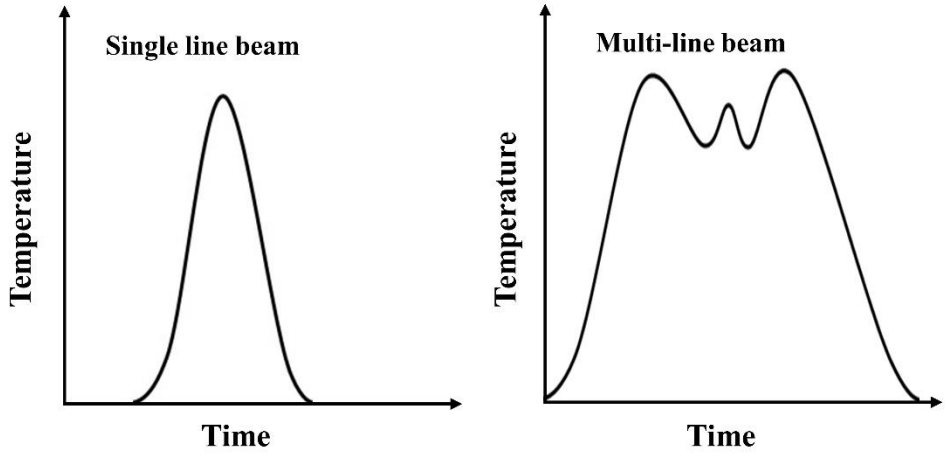

Fig. 5.2 Temperature profile of exposed regions: (a) single line beam, (b) multi-line beam.

Regarding overlapping scanning, the (100) textures can be seen at the restricted region of the laser power and scanning speed. At a single scan, the poly-Si film is distinguished by two areas resulting from a slight variation of laser density. The middle area of approximately 50% of 1100 μm irradiated width is dominated by (100) lateral-crystallized Si that is exposed at a higher energy density than the threshold. The side area is occupied by microcrystals and a-Si that is exposed at a lower energy density. The ratio of the lateral-crystallized Si area is enhanced as the energy is averaged by overlapping scanning. (100) crystal grains are hence formed in very large areas. The initial (100) orientation stage is unchanged as the film is re-irradiated because the orientation is mainly related to the absorbed energy of the Si. (I) As microcrystal region is re-irradiated at the higher energy density, they become lateral-recrystallized Si and oriented at the (100). (II) As the lateral-crystallized Si regions are re-irradiated, there are two possibilities: (1) The lateral-crystallized Si regions are not changed into molten phase as being overlapped by laser irradiation because the crystalline Si has a lower absorption coefficient at 532 nm waves and higher melting point than the a-Si [11]. (2) The crystalline Si is melted as it absorbs sufficient energy in spite of its lower laser absorption coefficient. However, the (100) preferential orientation is not changed because (100) texture formation is basically dependent on the laser energy. The (100) textures exists in a narrow range of the energy above the threshold for lateral-crystallized silicon. After being recrystallized, the poly-Si

is reoriented at the (100) because its absorbed energy is appropriate to the existent range of the (100) textures. The stability of (100) surface orientation with overlapping scanning demonstrates the (100) surface orientation control of the Si/SiO2 interfacial energy above the transition region. Otherwise, at overlapping scans, as crystalline Si is irradiated at these conditions, it is partially melted and then unmelted crystallites can be nuclei that control the orientation of their neighbors.

4.3 Mechanism of TFT's performance enhancement

In the chapter 4, we reported the crystallinities of the poly-Si channel of the ultrahigh mobility TFTs. It shows that the channel had (100) crystal grains parallel to its current flow. These TFTs can be considered as the sum of parallel (100) single Si crystal TFTs because the width of grain boundaries was negligible with the width of the channel. Moreover, their grain boundaries had small misorientation angles that generated a low grain boundary trap density. Figure 5.3 shows the example of the equivalent circuit of a parallel TFT including five crystal grains in the channel corresponding to five parallel TFTs.

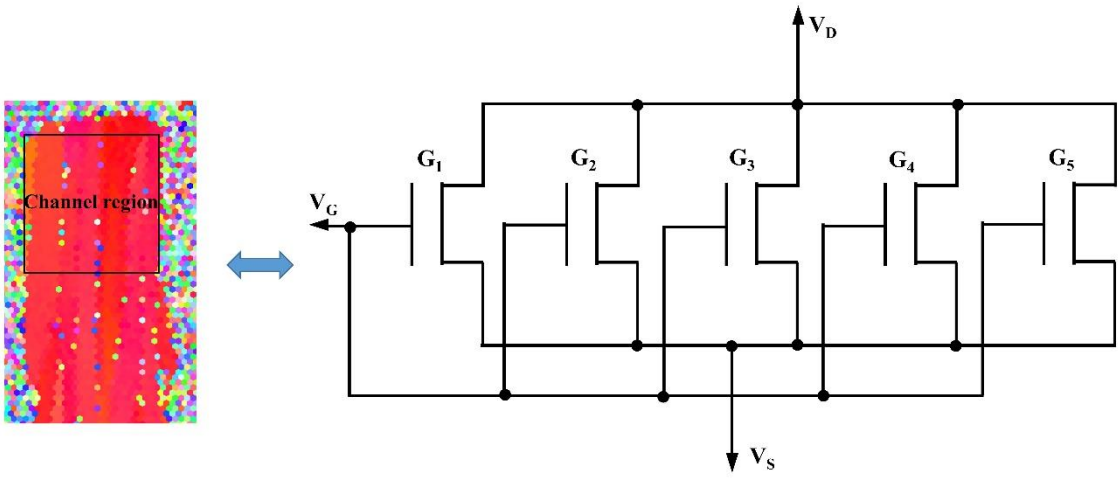

Fig. 5.3 Equivalent circuit of a parallel TFT

In addition, the poly-Si thin films had high biaxial tensile strain that significantly improved the electron mobility of the TFTs. In the chapter 2, we reported that the laser crystallized poly-Si thin films had a high compressive strain in the normal direction of -

0.4%. That is in turn the consequence of a biaxial tensile strain. From this result, tensile strain values in the scanning and transverse directions can be calculated.

With two-dimensional stress in the poly-Si thin films,

$$\sigma_X = \sigma_Y \equiv \sigma \tag{5.1}$$

The strains are given by the equations,

$$\varepsilon_X = \frac{\sigma}{E}(1 - \upsilon) \tag{5.2}$$

$$\varepsilon_Y = \frac{\sigma}{E}(1 - \upsilon) \tag{5.3}$$

$$\varepsilon_Z = \frac{2\sigma\upsilon}{E} \tag{5.4}$$

where σ is stress, ε_z is strain in out-of-plane direction, E is Young modulus, and υ is Poisson ratio. Silicon takes values as E = 160 GPa and υ = 0.279 [12-17].

With 1112 MPa average stress, the compressive strain in the normal direction and the tensile strain in in-plane directions are:

$$\varepsilon_Z = \frac{\sigma}{E}2\upsilon = \frac{1.112}{160} \times 2 \times 0.279 = 0.39\%$$

$$\varepsilon_X = \varepsilon_Y = \frac{\sigma}{E}(1 - \upsilon) = \frac{1.112}{160}(1 - 0.279) = 0.50\%$$

This value is good agreement with the result from the out-of-plane XRD spectrum.

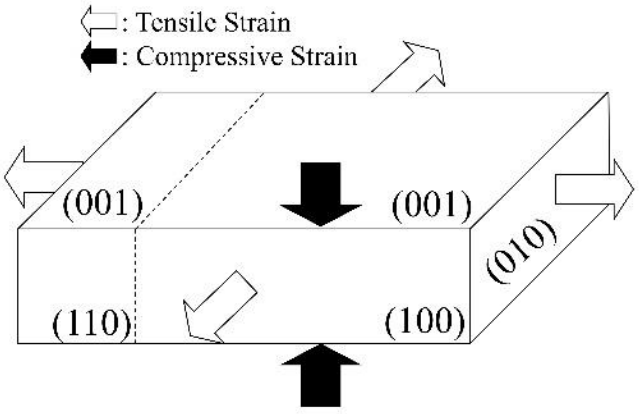

Fig. 5.4 Schematic of crystal structure of the (100) poly-Si

The schematic of crystal structure of the (100) poly-Si is shown in Fig. 5.4. The crystal orientation in the surface direction is (100), and the orientations in the laser scanning direction and the transverse direction are (100)-(100) or (110)-(110). The biaxial tensile strain was induced in the planar direction and on the contrary the compressive strain was induced in the depth direction. At (100) surface and <100> channel direction, the

electrons have a maximal mobility, then the TFT with this poly-Si film had a high mobility. And the biaxial strain enhances the mobility by reducing the effective mass in the planar direction, and the compressive strain in the depth direction makes the effective mass larger in this direction, and as a result the carrier electrons are confined in the surface of the poly-Si. As the net result, the electron mobility was significantly improved of approximately 50%. The mobility enhancement was discussed in the chapter 1. As the consequence of like-single Si(100) crystal TFTs with high biaxial tensile strain, the ultra-high-mobility of over 1000 cm^2/Vs was achieved.

4.4 Conclusions

This chapter discussed the mechanisms about the collected results in our research. Firstly, the mechanism of (100) texture formation with the MLB-CLC was clarified. With the results of (100) surface oriented poly-Si thin films formed at the crystallization conditions of above the transition region and comparing with the results and discussions in the previous reports, we believe that the SiO_2/Si interfacial energy control the surface orientation of the poly-Si thin film crystallized at low laser exposure energy regime. At high laser energy regime, this mechanism is inapplicable. Another mechanism for the (100) orientation preference being stable with the MLB shape is the possibility of the nucleation between line-beam exposures where the temperature of the poly-Si film is more uniform and these nuclei control the film oriented preferentially. Secondly, the mechanism of the stability of (100) surface orientation with overlapping scanning was shown. In this mechanism, the SiO_2/Si interfacial energy also play a very important role to keep the initial orientation unchanged. And thirdly, the mechanism of TFTs's performance enhancement was discussed. By examining the crystallinities of the poly-Si channel, we saw that the channel consisted of Si(100) single crystal grains parallel to the current flow and the poly-Si film had high biaxial tensile strain. It is believed that the TFTs' performance enhancement was brought about the like-single Si(100) crystal TFTs with high biaxial tensile strain poly-Si thin film.

References

[1] R. J. Jaccodine, "*Surface energy of Germanium and Silicon,*" J. The Electrochem. Soc., 524 (1963).

[2] A. A. Stekolnikov, J. Furthmuller, and F. Bechstedt, "*Absolute surface energies of group-IV semicondutors: Dependence on orientation and reconstruction,*" Phys. Rev. B **65**, 115318 (2002).

[3] S. Hong and M. Y. Chou, "*Effect of hydrogen on the surface-energy anisotropy of diamond and silicon,*" Phys. Rev. B **57**(11), 6262(1998).

[4] M. W. Geis, H. I. Smith, B-Y. Tsaur, J. C. C. Fan, D. J. Silversmith, and R. W. Mountain, "*Zone-Melting Recrystallization of Si Films with a Moveable-Strip-Heater Oven,*" J. Electrochem. Soc., 2812(1982).

[5] James S. Im, M. Chahal, P.C. van der Wilt, U.J. Chung, G.S. Ganot, A.M. Chitu, N. Kobayashi, K. Ohmori, A.B. Limanov, "*Mixed-phase solidification of thin Si films on SiO_2,*" J. Crys. Growth **312**, 2775(2010).

[6] N. Sasaki, Y. Nieda, D. Hishitani, Y. Uraoka, "*Power dependence of orientation on low-temperature poly-Si lateral grains crystallized by a continuous-wave laser scan,*" Thin Solid Films **631**, 112(2017).

[7] H. I. Smith, C.V. Thonpson, M. W. Geis, R. A. Lemons, and M. A. Bosch, "*The mechanism of orientation in Si graphoepitaxay by laser or strip heater recrystallization,*" J. Electrochem. Soc. **130**, 2050 (1983).

[8] Y. Wang, M. D. Chahai, J. J. Wang, A. B. Limanov, A. M. Chitu, J. S. Im, "*Analysis of Si-SiO_2 interfacial-energy hierarchy via mixed-phase solidification of Si films on SiO_2,*" Mater. Res. Soc. Symp. Proc. Vol. **1770**, pp. 55-60 (2015).

[9] J. Narayan, "*Interface structures during solid-phase-epitaxial growth in io-implanted semiconductors and a crystallization model*," J. Appl. Phys. **53**(12), 8067 (1982).

[10] L. Csepregi, E. F. Kennedy, and J. W. Mayer, "*Substrate-orientation dependence of the epitaxial regrowth rate from Si-implanted amorphous Si,"* J. Appl. Phys. **49**(7), 3906 (1978).

[11] S. Kuroki, Y. Kawasaki, S. Fujii, K. Kotani, "*Seed-Free Fabrication of Highly Bi-Axially Oriented Poly-Si Thin Films by Continuous-Wave Laser Crystallization with Double-Line Beams,*" J. Electrochem. Soc. **158**, H924 (2011).

[12] M. Janai, D. D. Allred, D. C. Booth, and B. O. Seraphin, "*Optical properties and structure of amorphous silicon films prepared by CVD,*" Solar Energy Materials **1**, 11(1979).

[13] Y. Okada and Y. Tokumaru, "*Precise determination of lattice parameter and thermal expansion coefficient of silicon between 300 and 1500 K,*" J. Appl. Phys., **56**, 314 (1984).

[14] J. J. Wortman and R. A. Evans, "*Young's Modulus, Shear Modulus, and Poisson's Ratio in Silicon and Germanium,*" J. Appl. Phys., **36**, 153 (1965).

[15] W. A. Brantley, "*Calculated elastic constants for stress problems associated with semiconductor devices,*" J. Appl. Phys. **44**, 534 (1973).

[16] H. Tada, A. Kumpel, R. E. Lathrop, J. B. Slanina, P. Nieva, P. Zavracky, I. N. Miaoulis, and P. Y. Wong, "*Thermal expansion coefficient of polycrystalline silicon and silicon dioxide thin films at high temperatures,*" J. Appl. Phys., **87**, 4189 (2000).

[17] H. Kahn, R. Ballarini, A. H. Heuer, "*Thermal Expansion of Low-pressure Chemical Vapor Deposition Polysilicon Films,*" J. Mater. Res. **17**, 1855 (2002).

Chapter 6: Conclusions and Future Work

This chapter gives a summary of this thesis and principle conclusions. Main contributions of this work are clarified and prospectively practical applications are discussed. Then, we suggest developable researches in the future.

6.1 Thesis conclusions

The objectives of this work are highly (100) oriented poly-Si thin film formation and high-performance LTPS-TFT fabrication.

In the chapters 2 and 3, we demonstrated (100) poly-Si thin films formed by using the MLB-CLC with single scans. Si(100) crystal grains developed along the laser scanning direction. They were relatively uniform and had a very large size of $20 \times 2\ \mu m^2$. The crystallization conditions for (100) texture formation were just above a threshold for lateral crystallized Si. At these conditions, the poly-Si thin films had (100) orientation in all surface, scanning, and transverse directions. By overlapping scanning, (100) textures were achieved in large areas. The poly-Si thin films had (100)-surface oriented crystals in large areas, dominantly. Moreover, the poly-Si thin films had a high bi-axial tensile strain in planar direction and a compressive strain in depth direction. The MLB-CLC poly-Si thin films generally had excellent orientation preference, large crystal grain size, well structural order that was comparable to the c-Si, and had high bi-axial tensile strain. We also investigate the effect of crystallization conditions including overlapping scanning, scanning speed, and laser power on the crystallinities of the laser- crystallized poly-Si films. We found that these conditions were major factors for the preferential orientation of the poly-Si thin films. The preferential orientation of the laser-crystallized poly-Si films was strongly dependent on the scanning speed and laser power and optimal conditions for (100) poly-Si thin films were clarified. These excellent crystallinities are great potentials that make the MLB-CLC a promising technology for high-performance TFTs.

In the chapter 4, we show the results of poly-Si TFTs fabricated with a low temperature process. Characterization of parallel and perpendicular TFTs was described, especially, parallel TFTs with ultrahigh-electron mobility were achieved on the highly (100) surface oriented poly-Si thin films. Approximately 1000 $cm^2V^{-1}s^{-1}$ electron field effect mobilities

are extremely high. The crystallinities of the poly-Si channels were characterized to evidence high mobility characteristics and orientation dependence of the mobility. High-performance perpendicular TFTs were also realized, they however had twice lower mobility than the parallel ones. Both parallel and perpendicular TFTs had high performance variation. In addition, a low hole field effect mobility was seen in the p-channel TFTs.

In chapter 5, the mechanisms for the above results were discussed. For (100) surface orientation, it is believed that the SiO_2/Si interfacial energy control the surface orientation of the poly-Si thin film crystallized at low laser exposure energy regime. Another possibility is the nucleation between line-beam exposures where the temperature of the poly-Si film is more uniform, and then these nuclei control the film oriented preferentially. Finally, we explained about the TFTs' performance enhancement and ultrahigh electron mobility achievement. By examining the crystallinities of the poly-Si channel, we saw that the channel consisted of Si(100) single crystal grains parallel to the current flow and the poly-Si film had high biaxial tensile strain. It is believed that the TFTs' performance enhancement was brought about the like-single Si(100) crystal TFTs with high biaxial tensile strain poly-Si thin film.

6.2 Future work

The above results bring me ideas to develop the MLB-CLC poly-Si TFTs for practical applications. For that reason, the disadvantages of high performance variation of the TFTs need to be improved. The variation is mainly brought about by the different orientation, grain boundaries, and voids in the poly-Si film. We have already formed uniformly (100) oriented poly-Si thin film without voids by adjusting the position of the laser optics and diffractive beam homogenizer for changing the laser beam configuration. In the next work, we will fabricate TFTs on those films. And to degrade the effect of grain boundaries, narrow channel TFTs would be developed in single crystal grains.

Acknowledgement

I would like to express my greatest gratitude to my supervisor, Associate Professor Shin-Ichiro Kuroki for his attentive guidance, continuous encouragement, and kind support throughout my research and the organization of this thesis. It is a great honor to be a PhD student in Graduate School of Advanced Science of Matter, Hiroshima University under his supervision. He did not only bring me a motivation and passion on research, but he also taught me facing to problems and resolving them. I am really grateful for his kindness.

I would like to express my deepest appreciation to Professor Shin-Yokoyama, Professor Han Jürgen Mattausch, and Professor Seiichiro Higashi for reviewing my doctoral thesis. Especially, the professors gave me valuable advices to improve my research during my academic years.

I would like to show my great thanks Professor Takamaro Kikkawa and Associate Professor Anri Nakajima for his discussions and advices on my research. I greatly appreciate Associate Professor Tetsuo Tabei and Assistant Professor Yoshiteru Amemiya for training and supporting me in operating apparatuses.

I would like to express my great gratitude to Professor Seiichiro Higashi and Assistant Professor Hiroaki Hanafusa for their kind support in my many EBSD measurements and SiO_2 deposition. These measurements and experiments are very important for my successful results.

I would like to show my deep thanks to Dr. Tomoyuki Koganezawa and Dr. Satoshi Yasuno for their kind support and discussions in 2D-XRD and HAXPES measurements and results.

I would like to thank all the memers of The Research Institute for Nanodevice and Bio Systems, especially the memers of Kuroki laboratory, for their support, discussions, and encouragement throughout my study and research.

I would like to thank Vietnamese Goverment for the financial support. I would like to express my deepest thank to all the members of Faculty of Physics, Hanoi National

University of Education, Vietnam for teaching, encouraging, and supporting me to pursue my dream.

I would like to show my whole-hearted thanks to my parents Nguyen Van Dung and Chu Thi An for their unconditional love and unfluctuating sacrifice. From the bottom of my heart, I appreciate my husband Do Minh Tuan and my son Do Dang Khoa who gave me the greatest love and moral force to make my dream come true.

Appendix

List of Publications and Award

Published papers

First author

[1] Ultrahigh-performance (100)-oriented polycrystalline silicon thin-film transistors and their microscopic crystal structures
Thi Thuy Nguyen, Mitsuhisa Hiraiwa, and Shin-Ichiro Kuroki
Applied Physics Express, **10**(5), 056501-1 -056501-4 (2017).

[2] Characterization of (100)-Dominantly Oriented Poly-Si Thin Film Transistors using Multi-Line Beam Continuous-Wave Laser Lateral Crystallization
Thuy Thi Nguyen, Mitsuhisa Hiraiwa, Tatsuaki Hirata, and Shin-Ichiro Kuroki
ECS Transactions, **75**(10), 49-54 (2016).

[3] Formation of (100) Oriented Large Poly-Si Thin Films with Multi-Line Beam Continuous-Wave Laser Lateral Crystallization
Thi Thuy Nguyen, Mitsuhisa Hiraiwa, Tomoyuki Koganezawa, Satoshi Yasuno, and Shin-Ichiro Kuroki
Japanese Journal of Applied Physics, **57**(3), 031302-1-031302-6 (2018).

Co-author

[1] Creating a Multiband Perfect Metamaterial Absorber at K Frequency Band Using Defects in the Structure
Manh Cuong Tran, Thi Thuy Nguyen, Tuan Hung Ho, and Hoang Tung Do
Journal of Electronic Materials, **46**(1), 413-417 (2016).

[2] Influence of Structural Parameters on a Novel Metamaterial Absorber Structure at K-band Frequency
Tran Manh Cuong, Nguyen Thi Thuy, and Le Anh Tuan
Journal of Electronic Materials, **45**(5), 2591-2596 (2016).

Presentation related to this thesis

International conferences

First author

[1] Ultrahigh-Performance Poly-Si Thin Film Transistor Using Multi-Line Beam Continuous-Wave Laser Lateral Crystallization
Thuy Thi Nguyen, Mitsuhisa Hiraiwa, Tatsuaki Hirata, and Shin-Ichiro Kuroki
The proceedings of The 23rd International Workshop on Active-Matrix Flat panel Displays and Devices (AM-FPD16), Vol. 4-3, pp. 277-279 (2016): Oral presentation

[2] Characterization of (100)-Dominantly Oriented Poly-Si Thin Film Transistors using Multi-Line Beam Continuous-Wave Laser Lateral Crystallization
Thuy Thi Nguyen, Mitsuhisa Hiraiwa, Tatsuaki Hirata, and Shin-Ichiro Kuroki,
PRiME 2016, The 230th Meeting of ECS, 2-7 October 2016, Hawaii, USA, H03-2118 (2016): Oral presentation

[3] Formation of Si(100)-Dominant Poly-Si Thin Film and Ultrahigh Performance Thin Film Transistors
Thuy Nguyen, Mitsuhisa Hiraiwa, and Shin-Ichiro Kuroki,
The 3rd International Symposium on Frontiers in Materials Science, 28-30 September 2016, Hanoi, Vietnam, pp. 68 (2016): Poster presentation

[4] Characterization of Ultra-High Performance Poly-Si Thin Film Transistors with (100)-Highly Oriented Poly-Si Film
Thi Thuy Nguyen, Mitsuhisa Hiraiwa, and Shin-Ichiro Kuroki
International Symposium on Biomedical Engineering, 10-11 November 2016, pp. 102-103 (2016): Poster presentation

[5] Characteristics of Ultra-High Performance Low-Temperature Thin Film Transistors with (100)-Highly Oriented Poly-Si Thin Films
Thi Thuy Nguyen, Mitsuhisa Hiraiwa, and Shin-Ichiro Kuroki,
International Workshop on Nanodevice Technologies 2017, 2 March, 2017, Hiroshima, Japan, pp. 68-69: Poster presentation

Co-author

[1] Back-side Illuminated GeSn Photodiode Array on Quartz Substrate Fabricated by Laser-induced Liquid-phase Crystallization for Monolithically-integrated NIR Imager Chip
H. Oka, K. Inoue, T. T. Nguyen, S. Kuroki, T. Hosoi, T. Shimura, and H. Watanabe,

2017 IEEE International Electron Devices Meeting (IEDM), 16.3 (2017)
Oral presentation

[2] (211) and (100) Surface Oriented Poly-Si Thin Film Transistors with Continuous-Wave Laser Lateral Crystallization (Invited)
Shin-Ichiro Kuroki, Thi Thuy Nguyen, and Mitsuhisa Hiraiwa
iMiD 2017, The 17th International Meeting on Information Display, BEXCO, Busan, Korea, 28-31 August, (2017)
Oral presentation.

[3] Charge-Trap Inactivation of Multi-Line-Beam CLC poly-Si TFTs using Channel Impurity Doping
M. Hiraiwa, T. T. Nguyen, S. I. Kuroki
PRiME2016, The 230th Meeting of ECS, Honolulu, USA, H03-2117 (2016)
Oral presentation.

[4] Poly-Si TFTs with One-dimensionally Long Silicon Crystal Grains Using DLB Continuous-wave Laser Lateral Crystallization (Invited)
Shin-Ichiro Kuroki, Tatsuaki Hirata, Nguyen Thuy Thi, Koji Kotani, and Takamaro Kikkawa,
iMiD 2015: The 15th International Meeting on Information Display, ISSN 1738-1558, Daegu, Korea, Aug. 18-21, 55-1, 250 (2015)
Oral presentation.

Domestic conferences

First author

[1] Si(100) crystal grains formation by Double-Line Beam Continuous-Wave Laser Lateral Crystallization with Overlapping
Thi-Thuy Nguyen and Shin-Ichiro Kuroki
The 76th JSAP Autumn Meeting, 13-16 September 2015, Nagoya, Japan, 15a-PB5-2 (2015) Poster presentation

[2] (100)-Dominantly Oriented Poly-Si Thin Films formed by Double-Line Beam Continuous-wave Laser Crystallization with Overlapping
Thi-Thuy Nguyen, Tatsuaki Hirata, and Shin-Ichiro Kuroki
The 12th Thin Film Materials and Devices Meeting, 30-31 October 2015, pp. 81-82 (2015) Poster presentation

[3] Poly-Si thin film transistor on (100)-dominantly Si film using MLB-CLC with overlapping
Nguyen Thuy Thi, Hirata Tatsuaki, Kuroki Shin-Ichiro
The 63rd JSAP Spring Meeting, 19-22 March 2016, Tokyo, Japan, 19a-S224-2 (2016) Oral presentation

[4] Characterization of (100) Surface Oriented Poly-Si Film using Multi-line Beam Continuous-wave Laser Lateral Crystallization
Nguyen Thuy Thi, Mitsuhisa Hiraiwa, Tomoyuki Koganezawa, Satoshi Yasuno, and Shin-Ichiro Kuroki
The 78th JSAP Autumn Meeting, 5-8 September, 2017, Fukuoka, Japan, 7a-C21-12 (2017) Oral presentation

[5] Void-Location Control of (100) Oriented Laser-Crystallized Large Poly-Si Thin Films
Thi-Thuy Nguyen, Mitsuhisa Hiraiwa, and Shin-Ichiro Kuroki
The 14th Thin Film Materials and Devices Meeting, 20-21 October 2017, pp. 152-154 (2017) Poster presentation

Co-author

[1] Origin of Donor-type defects in MLB-CLC poly-Si TFTs
M. Hiraiwa, T. T. Nguyen, and S-I. Kuroki
The 14th Thin Film Materials and Devices Meeting, 20-21 October 2017, pp. 43-44 (2017)
Oral presentation

[2] Effect of channel doping on poly-Si TFTs with Multi-Line-Beam CLC
Mitsuhisa Hiraiwa, Tatsuaki Hirata, NguyenThi Thuy, Koji Kotani, Shin-Ichiro Kuroki
The 63th JSAP Spring Meeting, 19-22 March 2016, Tokyo, Japan 21p-P17-3 (2016)
Poster presentation

[3] Effect of grain boundary on electrical characteristics of low-temperature MLB-CLC poly-Si TFTs
Tatsuaki Hirata, Nguyen Thuy, Mituhisa Hiraiwa, Koji Kotani, Takamaro Kikkawa, Shin-Ichiro Kuroki
The 63th JSAP Spring Meeting, 19-22 March 2016, Tokyo, Japan, 21p-P17-4 (2016)
Poster presentation

Awards

平成 28 年度広島大学先端物質科学研究科半導体集積科学専攻エクセレント・スチューデント・スカラシップ

公表論文

(1) Ultrahigh-performance (100)-oriented polycrystalline silicon thin-film transistors and their microscopic crystal structures
Thi Thuy Nguyen, Mitsuhisa Hiraiwa, and Shin-Ichiro Kuroki
Applied Physics Express, **10**(5), 056501-1 -056501-4 (2017).

(2) Characterization of (100)-Dominantly Oriented Poly-Si Thin Film Transistors using Multi-Line Beam Continuous-Wave Laser Lateral Crystallization
Thuy Thi Nguyen, Mitsuhisa Hiraiwa, Tatsuaki Hirata, and Shin-Ichiro Kuroki
ECS Transactions, **75**(10), 49-54 (2016).

(3) Formation of (100) Oriented Large Poly-Si Thin Films with Multi-Line Beam Continuous-Wave Laser Lateral Crystallization
Thi Thuy Nguyen, Mitsuhisa Hiraiwa, Tomoyuki Koganezawa, Satoshi Yasuno, and Shin-Ichiro Kuroki
Japanese Journal of Applied Physics, **57**(3), 031302-1-031302-6 (2018).

参 考 論 文

(1) Creating a Multiband Perfect Metamaterial Absorber at K Frequency Band Using Defects in the Structure
Manh Cuong Tran, Thi Thuy Nguyen, Tuan Hung Ho, and Hoang Tung Do
Journal of Electronic Material**s, 46(**1**),** 413-417 (2016).

(2) Influence of Structural Parameters on a Novel Metamaterial Absorber Structure at K-band Frequency
Tran Manh Cuong, Nguyen Thi Thuy, and Le Anh Tuan
Journal of Electronic Materials, **45**(5), 2591-2596 (2016).